RBPMS2 is a conserved regulator of alternative splicing that promotes myofibrillar organization and optimal calcium handling in cardiomyocytes

Alexander A. Akerberg[1,2,3], Michael Trembley[1,3], Vincent Butty[4], Asya Schwertner[2,3], Long Zhou[2,3] Manu Beerens[2,3,5], Xujie Liu[1,3], Mohammed Mahamdeh[2,3], Shiaulou Yuan[2,3], Calum MacRae[3,5], Christopher Nguyen[2,3], William T. Pu[1,3,6], Caroline E. Burns[1,2,3,6*], C. Geoffrey Burns[1,2,3*]

[1] Division of Basic and Translational Cardiovascular Research, Department of Cardiology, Boston Children's Hospital, Boston, MA, USA
[2] Cardiovascular Research Center, Massachusetts General Hospital, Charlestown, MA, USA
[3] Harvard Medical School, Boston, MA, USA
[4] Department of Biology, Massachusetts Institute of Technology, Cambridge, MA, USA
[5] Division of Cardiovascular Medicine, Brigham and Women's Hospital, Boston, MA, USA
[6] Harvard Stem Cell Institute, Cambridge, MA, USA

* Correspondence: caroline.burns@childrens.harvard.edu, geoff.burns@childrens.harvard.edu

Key Words: Heart disease, cardiomyopathy, alternative splicing, zebrafish, human cardiomyocytes, *rbpms2*, *mybpc3*, *pln, slc8a1a.*

SUMMARY

The identification of novel cardiomyocyte-intrinsic factors that support ventricular function will expand the number of candidate genes and therapeutic options for heart failure, a leading cause of death worldwide. Here, we demonstrate that a conserved RNA-binding protein RBPMS2 is required for ventricular function in zebrafish and for myofibril organization and the regulation of intracellular calcium dynamics in zebrafish and human cardiomyocytes. A differential expression screen uncovered co-expression of *rbpms2a* and *rbpms2b* in the zebrafish myocardium. Double knockout embryos suffer from compromised ventricular filling during the relaxation phase of the cardiac cycle, which significantly reduces cardiac output. RNA-sequencing analysis and validation studies revealed differential alternative splicing of the cardiomyopathy genes myosin binding protein C3 (*mybpc3*) and phospholamban (*pln*) in *rbpms2*-null embryos. Cardiomyocytes in double mutant ventricles and those derived from *RBPMS*2-null human induced pluripotent stem cells exhibit myofibril disarray and calcium handling abnormalities. Taken together, our data suggest that *RBPMS2* performs a conserved role in regulating alternative splicing in cardiomyocytes, which is required for myofibrillar organization, optimal calcium handling, and cardiac function.

INTRODUCTION

Heart failure remains a common, costly, and growing public health burden (Virani et al., 2021). While lifestyle choices that cause hypertension and myocardial infarction are substantial contributors to heart failure, inherited and *de novo* genetic mutations that cause primary diseases of the heart muscle, including hypertrophic cardiomyopathy (HCM) and dilated cardiomyopathy (DCM) are also important instigators of disease (Garfinkel et al., 2018; Skrzynia et al., 2014). Causal mutations for HCM and DCM commonly reside within two classes of genes, those encoding components of the sarcomere, the basic contractile unit of cardiac muscle, and those encoding factors that regulate calcium handling, another critical determinant of cardiac contractility (Gorski et al., 2015; Skrzynia et al., 2014; Towbin, 2000; Towbin and Bowles, 2000). While the pathogenesis of mutations affecting sarcomeres and calcium handling is well-established in HCM and DCM, a significant percentage of cases remain idiopathic, because clinically recognized cardiomyopathy susceptibility genes remain mutation free in targeted sequencing panels. Therefore, ongoing efforts to identify novel molecular activities required for optimal myocardial contractility will highlight novel candidate genes for primary cardiomyopathies.

Alternative mRNA splicing has emerged in recent years as an important regulator of myocardial contractility in humans. Disruptions in the RNA-recognition motif (RRM)-containing protein RBM20 were recently discovered to cause dilated cardiomyopathy (DCM) by regulating alternative splicing of TITIN (TTN), the largest protein component of the sarcomere (Guo et al., 2012; Hoogenhof et al., 2018; Maatz et al., 2014). TTN transcripts within the heart can be separated into three distinct classes, each of which codes for a unique combination of functional domains (LeWinter and Granzier, 2013). Loss of Rbm20 in animal models results in aberrant splicing of TTN, leading to changes in ventricular morphology and diminished contractility in a manner consistent with observations in DCM patients. Clinical studies have further confirmed that genetic variation in the Rbm20 locus is associated with a higher risk of cardiomyopathy

(Haas et al., 2015; Refaat et al., 2012). Alternatively, spliced transcripts of calcium/calmodulin-dependent kinase II delta (CAMK2D) were also shown to contribute to increased risk of arrhythmogenic cardiomyopathy in the absence of Rbm20 (Hoogenhof et al., 2018), demonstrating roles for Rbm20 in the regulation of myocardial calcium handling and action potential propagation. Similar to Rbm20, another RRM-containing protein, termed Rbm24, was shown to regulate the splicing of a subset of genes encoding components of the sarcomere, including TTN, within postnatal mice(Liu et al., 2019). Initial screens for Rbm24 mutations in human cardiomyopathy patients suggest a potential link to disease, however, these mutations were found to be relatively rare in the disease population (Gaertner et al., 2019). Together these data represent the first etiological links between splicing factors and cardiomyopathy, thereby underscoring the importance for further research to identify the full array of splicing factors that regulate cardiac form and function.

The importance of alternative splicing in the heart is further evidenced by the abundance of isoform variation within cardiac-specific transcripts. Furthermore, many genes with established roles in cardiomyopathy are known to produce multiple distinct isoforms within the heart. For example, the cardiac troponin t (*TNNT2*) gene is alternatively spliced in a regulated pattern during cardiac development and aberrant splicing can lead to cardiomyopathy in animal models (Biesiadecki et al., 2002; Farza et al., 1998; Jin and Lin, 1989). Other cardiomyopathy genes such as tropomyosin (*TPM1*) and myosin binding protein C3 (*MYBPC3*) are predicted to be alternatively spliced in a similar fashion, however the importance of these splicing events and the identity of the factors that govern them remain unknown.

Here, we identify the RRM-containing protein Rbpms2 (RNA binding protein with multiple splicing 2) as a crucial regulator of alternative splicing within the developing myocardium. We show that Rbpms2a and Rbpms2b redundantly promote ventricular contractility within the developing zebrafish heart. Further, we show that these Rbpms2 proteins regulate the splicing of numerous genes that are associated with cardiac sarcomere assembly and ion transport,

including transcripts for known disease genes *mybpc3* and *phospholamban* (*pln)* (MacLennan and Kranias, 2003; Niimura et al., 1998). We then demonstrate that *rbpms2*-null animals exhibit sarcomere disorganization and calcium handling deficits that are consistent with the misregulation of Rbpms2 targets.

RESULTS

Differential expression analysis of FACS-purified zebrafish anterior lateral plate mesodermal cells identifies cardiomyocyte-restricted expression of rbpms2a and rbpms2b

Lineage-restricted genes often perform specialized and essential functions in the development, maintenance, or function of the populations they mark. To generate a candidate list of zebrafish genes with essential activities in cardiopharyngeal progenitors or embryonic cardiomyocytes, we sought to identify mRNAs with restricted expression to the subset of anterior lateral plate mesodermal (ALPM) cells marked by the *nkx2.5:ZsYellow* transgene. This population contains cardiopharyngeal progenitors for multiple cell types including second heart field-derived ventricular cardiomyocytes, three outflow tract (OFT) lineages, a subset of pharyngeal muscles, and endothelium of the pharyngeal arch arteries (Guner-Ataman et al., 2013; Paffett-Lugassy et al., 2013; Schoenebeck et al., 2007; Serbedzija et al., 1998; Zhou et al., 2011). It also contains early-differentiating ventricular cardiomyocytes derived from the first heart field (Guner-Ataman et al., 2013; Schoenebeck et al., 2007; Serbedzija et al., 1998).

To isolate ALPM cells labeled with the transgene, *Tg(nkx2.5:ZsYellow)* embryos were dissociated to single cells at a developmental stage when ZsYellow fluorescence is restricted to the ALPM [14-16 somites stage (ss); Fig. 1A]. Dissociated cells were separated by FACS into ZsYellow-positive and ZsYellow-negative subpopulations before being subjected to RNA-sequencing and differential expression analysis (Fig 1A; Fig S1A-C). From this, we identified 1848 protein-coding RNAs significantly enriched in the ZsYellow-positive population [fold change (FC)>1.5; adjusted p-value<0.05; Fig. 1A; Fig. S1D; Table S1]. Among them were

several previously characterized lateral plate mesodermal markers that encode transcription factors essential for vertebrate cardiopharyngeal development including *nkx2.5*, *hand2*, *gata4/5/6*, *mef2ca/b*, *tbx1/5a/20*, *isl1*, and *fgf8a/10a/10b* (Fig. S1D; Table S1). Due to the presence of early-differentiating cardiomyocytes in the ZsYellow-positive population, we also identified numerous genes encoding sarcomere components [*cmlc1*, *myl7* (*cmlc2*), *myh7* (*vmhc*), *myh6* (*amhc*), *acta1b*, *actc1a*, *actn2b*, *tnni1b*, *tnnt2a, tnnc1a, tpm4a, ttn.2*], calcium handling proteins [*slc8a1a* (*ncx1*), *ryr2b, atp2a2a (serca2)*] and other factors expressed preferentially in cardiomyocytes (*cx36.7*, *nppa/al/b*; Fig. S1D; Table S1). Not surprisingly, gene ontology (GO) term enrichment analysis uncovered overrepresentation of biological process terms “heart development”, “angiogenesis”, “heart contraction”, “actin cytoskeletal organization”, and “sarcomere organization” in the ALPM-enriched gene set (Fig. S1E, see Table S1 for complete GO term analysis). The successful identification of ALPM markers with well-documented and indispensable roles in cardiopharyngeal progenitors or cardiomyocytes suggests that novel molecular activities of equal importance are likely to be among the uncharacterized ALPM-restricted genes.

Transcripts encoding RNA binding protein with multiple splicing (variants) 2a (Rbpms2a) and Rbpms2b were enriched 14- and 5-fold, respectively, in the ZsYellow-positive population (Fig. S1D; Table S1), suggesting that these RNA-recognition motif (RRM)-containing proteins localize to the ALPM. Classified as ohnologs, *rbpms2a* and *rbpms2b* encode proteins that are 92% identical and perform redundant functions in oocyte differentiation (Kaufman et al., 2018). Across the full-length amino acid sequences, Rbpms2a and Rbpms2b share greater than 81% identity with human RBPMS2 (Fig. S2A,B). The shared identity exceeds 92% in the RRMs (Fig. S2A,B). Such a high degree of sequence conservation suggests that the molecular function of RBPMS2 proteins and the properties of their binding site sequences are also likely to be conserved across evolution.

The founding member of the *RBPMS2* gene family, originally termed *hermes*, was discovered in a differential expression screen designed to identify heart-specific transcripts in *Xenopus* (Akerberg et al., 2019a; Gerber et al., 1999). In situ hybridization revealed that *RBPMS2* localizes to the lateral plate mesoderm and embryonic myocardium in both amphibian and avian species (Gerber et al., 1999; Wilmore et al., 2005). Hearts of embryonic zebrafish were also recently reported to express *rbpms2a* and *rbpms2b* (Kaufman et al., 2018). Despite the high degree of amino-acid sequence conservation and consistent myocardial-restricted expression pattern across vertebrates, *RBPMS2* has yet to be implicated in any aspect of myocardial biology through genetic loss-of-function studies.

To validate the predicted ALPM localization of *rbpms2a* and *rbpms2b,* we performed in situ hybridization for both genes at the same developmental stage used for profiling *nkx2.5:ZsYellow*-positive ALPM cells (16 ss; Fig. S1). As anticipated, both transcripts localized bilaterally to the ALPM (Fig. 1B,E) in a pattern mirroring early-differentiating cardiomyocytes in at this stage (Yelon et al., 1999). Later-stage analysis revealed *rbpms2a* and *rbpms2b* expression in the heart tube at 24-28 hours post fertilization (hpf; Fig. 1C,F; Fig. S3A,C) and in the atrium and ventricle of the two-chambered heart at 48 hpf (Fig. 1D,G; Fig. S3B,D). Consistent with previous reports (Hörnberg et al., 2013; Kaufman et al., 2018), extra-cardiac expression was observed in the pronephric duct and retina (Fig. S3A-D)

To investigate the lineage specificity and subcellular localization of Rbpms2a and Rbpms2b in the zebrafish heart, we immunostained wild-type embryos with a monoclonal antibody raised against human RBPMS2, which cross reacts with zebrafish Rbpms2 (see below). Consistent with the distribution of *rbpms2a/b* transcripts, Rbpms2 protein was detected in the heart tube (Fig. 1H,I; Fig. S3E,F), two chambered heart (Fig. 1J,K; Fig. S3G), pronephric duct (Fig. S3E-G) and retina (Fig. S3F,G). Double-immunostaining for Rbpms2 and the myocardial marker cardiac Troponin T (CT3) revealed that Rbpms2 expression localizes to the myocardium at all stages analyzed (Fig. 1H’,I’,J’,K’). Weak expression of Rbpms2 was also

evident by 72 hpf in the OFT (i.e. bulbous arteriosus; Fig. 1K,K'). Examination of single optical sections through the ventricular wall, which showed nuclear Rbpms2 signals surrounded by Troponin T-positive cytoplasm, confirmed myocardial localization of Rbpms2, (Fig. 1L-L'''). Adjacent endocardial cells were devoid of Rbpms2 signals, which highlights the myocardial-specific nature of Rbpms2 expression (Fig. 1L-L'''). The subcellular distribution of Rbpms2 appeared variable, ranging from a nucleocytoplasmic distribution to exclusively nuclear (Fig. 1H,I,J,K), but the significance of this observation is unknown. Lastly, we documented Rbpms2 expression in the nuclei and cytoplasm of cardiomyocytes in hearts from adult zebrafish (Fig. 1M,M'), suggesting that Rbpms2 functions in the myocardium continuously throughout the lifespan of zebrafish rather than transiently during embryogenesis.

Generation of Rbpms2-null zebrafish

To discover if *rbpms2a* and *rbpms2b* are required for myocardial development or function, we created mutant alleles of both genes using transcription activator-like effector nucleases (TALENs) (Sander et al., 2011). TALEN pairs were designed to target DNA sequences encoding N-terminal regions of the RRM domains (Fig. S4A,B). We isolated the mutant alleles *rbpms2a*^{chb3} and *rbpms2b*^{chb4}, which carry frame-shifting deletions and premature stop codons that truncate the proteins by >80% (Fig. 2A,B; Fig. S4A,B). The truncations also remove 82% of the RRMs, suggesting that the RNA-binding activities of the mutant proteins are abolished or significantly compromised. As a result, both alleles are likely to be null. Animals homozygous for either *rbpms2a*^{chb3} or *rbpms2b*^{chb4} are grossly indistinguishable from siblings during all life stages, which is consistent with a previous study that independently generated mutant alleles of *rbpms2a* and *rbpms2b* (Kaufman et al., 2018).

To determine if *rbpms2a* and *rbpms2b* perform redundant functions in the heart, we generated and monitored double homozygous embryos [i.e. *rbpms2a*$^{chb3/chb3}$*; rbpms2b*$^{chb4/chb4}$ animals, referred to hereafter as *rbpms2*-null, double-mutant, or double-knockout (DKO)

embryos or animals] for cardiac defects. DKO animals are grossly indistinguishable from control siblings for the first ~30 hours of life. By ~33 hpf, they develop a characteristic indentation of the yolk, which is indicative of mild pericardial edema (Fig. S4C,D). At this stage, double-mutants are delayed in initiating blood flow even though peristalsis of the heart tube is readily evident. By 72 hpf, pericardial edema becomes progressively more severe (Fig. 2C,D), suggesting that *rbpms2*-null animals suffer from a cardiac malformation or ongoing functional deficit.

Western blotting and whole mount immunostaining revealed that the zebrafish epitopes recognized by the anti-human RBPMS2 antibody are completely absent in double mutants (Fig. 2E-G), demonstrating that the antibody cross reacts with zebrafish Rbpms2. It also suggests that the mutant mRNAs or proteins are unstable, further suggesting that *rbpms2a*^{chb3} and *rbpms2b*^{chb4} are bona fide null alleles.

To assess double-mutant viability, we monitored the survival of control-sibling and DKO animals from embryonic stages to adulthood. Over 50% of *rbpms2*-null animals died by two weeks of age (Fig. 2H). Eighty five percent of animals perished by 60 days post fertilization (dpf), and the remaining small percentage of animals did not survive beyond 6 months post fertilization. At all ages, death was generally accompanied by progressively severe pericardial edema, suggesting a cardiac origin.

rbpms2a and rbpms2b are required for chamber expansion during ventricular filling

To evaluate DKO embryos for structural heart disease, we examined hearts in 48 hpf control-sibling and *rbpms2*-null animals carrying the *myl7:GFP* transgene, which labels the entire myocardium with GFP. Although the two-chambered heart in double mutants displayed normal left-right patterning, the ventricle was displaced anteriorly relative to the atrium (Fig. 2I,J), likely reflecting stretching at the cardiac poles caused by pericardial edema. Atrial size was not obviously altered in *rbpms2*-null animals, but mutant ventricles appeared smaller (Fig.

1I,J). To determine if this might reflect a diminished ventricular cardiomyocyte number, we quantified cardiomyocytes in control-sibling and *rbpms2*-null animals carrying the *myl7:nucGFP* transgene, which labels cardiomyocyte nuclei with GFP (Fig. 2K,L). From this, we learned that ventricular, as well as atrial, cardiomyocyte numbers were unaltered in double mutants (Fig. 2K-M; Fig. S5A), demonstrating that any deviations in chamber size are not attributable to altered myocardial cell content. It also suggests that *rbpms2a* and *rbpms2b* are dispensable for myocardial differentiation from the first and second heart fields, which is the principal method by which cardiomyocytes are produced before 48 hpf (Hami et al., 2011; Lazic and Scott, 2011; Pater et al., 2009; Zhou et al., 2011). These data demonstrate that early cardiac morphogenesis is largely unperturbed in double mutant animals, with the only apparent anatomical abnormality being a reduction in ventricular size.

To characterize potential functional defects in *rbpms2*-null hearts, we measured ejection fraction and cardiac output in 48 hpf animals using our previously-described Cardiac Functional Imaging Network [CFIN; (Akerberg et al., 2019b)]. To that end, we captured Z-stack dynamic images of GFP+ hearts over several cardiac cycles in control-sibling and DKO *myl7:GFP* transgenic embryos using light sheet fluorescence microscopy. CFIN extracted chamber volumes and identified the maximum and minimum ventricular volumes throughout the cardiac cycle, referred to as end-diastolic volume (EDV; maximum volume during cardiac relaxation) and end-systolic volume (ESV; minimum volume during cardiac contraction), respectively. Whereas the ESV was unchanged in DKO animals, the EDV was significantly reduced (Fig. 2N-R), demonstrating that the ventricle fails to expand during the relaxation phase of the cardiac cycle. As a result, three indices of ventricular function, all of which are calculated from EDV and ESV, were significantly reduced. These include stroke volume (SV), the volume of blood expelled by the ventricle per beat (SV=EDV-ESV), ejection fraction, the percentage of blood expelled by the ventricle per beat (EF=SV/EDV), and cardiac output, the total volume of blood expelled by the ventricle per minute (SV*heart rate) (Fig. 2R). Heart rate was unchanged in the

mutant (Fig. 2R). CFIN analysis also revealed an increase in atrial volume (Fig. S5B), which was not grossly obvious after fixation (Fig. 2I,J) and is a common secondary consequence of impaired ventricular function (Cuspidi et al., 2011, 2013; Huttner et al., 2018). These data demonstrate that *rbpms2a* and *rbpms2b* are required for ventricular function in the zebrafish embryo. This requirement likely extends into adulthood because the longest-living double-mutant animals exhibited several signs of heart failure such as stunted growth, pericardial edema, and cardiac pathologies including compact, fibrotic ventricles and massively enlarged atria (Fig. S6A-E).

Identification of differential alternative splicing events in rbpms2-null zebrafish

To identify transcriptomic abnormalities in the hearts of *rbpms2*-null embryos, we performed bulk RNA-sequencing and differential expression analysis on control-sibling and *rbpms2*-null animals at 33 hpf, the earliest developmental stage when DKO animals are distinguishable by morphology (Fig. S4C,D). We reasoned that early-stage analysis would maximize the chances of highlighting primary molecular defects without interference by secondary responses to cardiac dysfunction. Importantly, we confirmed that the primitive ventricle in 33 hpf *rbpms2*-null animals exhibits a functional deficit by documenting reduced myocardial wall movement at the arterial pole of the heart tube (Fig. S7A). We also confirmed that total cardiomyocyte numbers are unaltered at 33 hpf in double mutants (Fig. S7B), reducing the chances that any transcriptomic abnormalities would be attributable to altered cellular composition. Lastly, we profiled whole embryos, instead of purified hearts, because effective protocols for isolating hearts or cardiomyocytes at this early stage do not currently exist. Nonetheless, because *rbpms2a* and *rbpms2b* are expressed with exquisite specificity in the heart, retina and pronephric duct (Fig. S3F), we anticipated that the transcriptional changes occurring in the myocardium would be a discernable subset of those occurring in the whole animal.

While RNA-sequencing and gene-level differential expression analysis highlighted only 2 downregulated transcripts in *rbpms2*-null animals (|FC|>1.5; p-adj<0.05; Table S2; Figure S8A), isoform-level differential expression analysis yielded 78 downregulated and 74 upregulated transcripts (|FC|>1.5; p-adj<0.05; Table S3; Fig. S8B). GO term analysis did not identify overrepresentation of any terms in either gene set [False Discovery Fate (FDR)<0.05]. However, among the downregulated transcripts, there were three well-characterized myocardial genes including *phospholamban* (*pln*; FC=-43.00; p-adj=1.53E-09), *atrial myosin heavy chain 6* (*myh6*; FC=-2.17; p-adj=1.52E-11), and *natriuretic peptide precursor a* (*nppa*; FC=-1.57; p-adj=0.019; Fig. S8B; Table S2). We confirmed downregulation of *nppa* by reverse-transcription quantitative PCR (RT-qPCR) at 33hpf (Fig. S7C). However, this reduction was short lived because two subsequent developmental stages showed increased *nppa* expression (Fig. S7C), which is characteristic behavior for *nppa* in response to cardiac stress (Horsthuis et al., 2008). RT-qPCR analysis of *myh6* revealed a downward trending but statistically insignificant change in double mutants (Fig. S7D). Ultimately, downregulation of either gene is unlikely to explain the ventricular phenotype in *rbpms2*-null mutants because *nppa*-null zebrafish do not exhibit any gross cardiac defects (Grassini et al., 2018) and the primary defect in *myh6*-deficient animals is a silent atrium (Berdougo et al., 2003).

Of the two *pln* genes in the zebrafish genome (GRCZ11), *si:ch211-270g19.5* (ENSDARG00000097256) and *pln* (ENSDARG00000069404), the latter is alternatively spliced according to publicly available cDNA sequencing data. Interestingly, only one of the alternatively-spliced *pln* isoforms (ENSDART00000141159; *pln-203*) was found to be downregulated in *rbpms2*-null animals (FC=-43.00; p-adj1.53E-09; Fig. S8B; Table S2). The other *pln* transcript (ENSDART00000133911**;** *pln-202***)** was unchanged (FC=1.37; p-adj>0.99; Table S2), which highlighted the possibility that Rbpms2 functions in the zebrafish myocardium to regulate alternative splicing, a molecular function previously ascribed to the closely related RBPMS protein (Nakagaki-Silva et al., 2019), but not to RBPMS2 itself (Akerberg et al., 2019a).

To investigate this possibility directly, we performed replicate multivariate analysis of transcript splicing (rMATS) (Shen et al., 2014) on the same RNA-sequencing dataset and identified 150 differential alternative splicing events (ASEs) in *rbpms2*-null animals (0 uncalled replicates; FDR<0.01; |Incleveldifference|>0.1; Fig. 3A,B; Table S3). The most common ASE was skipped exon (SE), representing over 40% of the total ASEs, followed by alternative 3' splice site (A3SS, 23%), alternative 5' splice site (A5SS, 21%), mutually exclusive exons (MXE, 10%), and retained intron (RI, 6%) (Fig 3A,C). Gene ontology (GO) term enrichment analysis did not identify overrepresentation of any terms among the differentially spliced genes. However, a limited number of myocardial genes were found to be differentially spliced in *rbpms2*-null animals including *myosin binding protein C3* (*mybpc3*) and *myomesin 2a* (*myom2a*), both of which encode sarcomere components (Agarkova and Perriard, 2005; Gautel and Djinović-Carugo, 2016; Previs et al., 2012, 2015), and *solute carrier family 8 member 1a* [*slc8a1a*; also termed the *sodium calcium exchanger 1* (*ncx1*)] which encodes a plasma membrane transporter responsible for extruding calcium from cardiomyocytes during cardiac relaxation (Ebert et al., 2005; Langenbacher et al., 2005).

In the case of *mybpc3*, exons 2 and exons 10 were identified as cassette exons whose inclusion levels (Inclevels) in mature *mybpc3* transcripts were found to be significantly lower in *rbpms2*-null animals (exon2 Inclevel=0.031; exon 10 Inclevel=0.057) when compared to those in control siblings (exon2 Inclevel=0.557; exon10 Inclevel =0.296; exon 2 Incleveldifference=0.526, FDR=4.77E-40; exon 10 Incleveldifference=0.24, FDR=2.38E-21; Fig. 3B; Fig.4A; Table S4). The same was true for exon 16 of *myom2a* (control Inclevel=1, DKO Inclevel=0, Incleveldifference=1, FDR 2.74E-20; Fig. 3B; Fig.4A; Table S4) and exon 5 of *slc8a1a* (control Inclevel=1, DKO Inclevel=0.37, Incleveldifference=0.629, FDR=4.92E-14; Fig. 3B; Fig.4A; Table S4). In all cases, exon inclusion was higher in in control siblings, which means that these exon sequences were significantly reduced or absent in *rbpms2*-null animals.

Despite supporting evidence from differential isoform expression analysis (Fig. S8B; Table S2), rMATS did not identify alternative splicing of *pln*, likely because it involves a terminal exon (Fig. 4A), which rMATS is not designed to evaluate (Fig. 3A). Therefore, we employed the mixture of isoforms (MISO) algorithm (Katz et al., 2010) to evaluate alternative splicing of *pln* in *rbpms2*-null animals and found strong statistical evidence that the exon 3-containing *pln*-203 isoform (ENSDART00000141159) is uniquely reduced in mutant animals. Specifically, the Bayes factor was largely above the accepted cutoff of 5 for differences in ENSDART00000141159 versus ENSDART00000133911 usage in WT and double-mutant animals across all five replicate pairs (Table S5), which is strongly suggestive of differential alternative splicing. This conclusion was also supported by genotype-specific differences in read densities across the locus (Fig. S9).

Validation of differential alternative splicing events in rbpms2-null zebrafish

Next, we used splicing-sensitive RT-qPCR to validate differential alternative splicing of *mybpc3*, *myom2a*, *slc8a1*, and *pln* in *rbpms2*-null animals at 48 hpf (Fig. 4A). To that end, we designed two primer pairs for each transcript. One was designed to measure relative “total transcript” levels between sibling control and *rbpms2*-null animals, independent of the alternatively spliced exon. The other was designed to quantify relative “isoform-specific” levels by having one of the primer-binding sites contained within the exon of reduced inclusion according to rMATS or MISO (Fig. 4A). For all four genes, total transcript levels were not significantly altered in *rbpms*2-null animals (Fig. 4B). However, the specific exon-containing isoforms were reduced by at least 50% in all cases, and by greater than 95% in three cases, indicative of almost-complete exon exclusion (Fig. 4C). Taken together, these data provide strong evidence that Rbpms2 activity promotes the inclusion of specific exons into mature cardiac transcripts. Importantly, we verified that *mybpc3* and *pln* are also abnormally spliced earlier in development (33 hpf), when signs of cardiac distress first become visible in double

mutants, reducing the likelihood that abnormal splicing is a secondary consequence of cardiac dysfunction (Fig. S7E,F).

To confirm that the DKO splicing abnormalities localize to the myocardium, we performed splicing-sensitive in situ hybridization analysis for two genes, *mybpc3* and *pln*, with *rbpms2*-dependent exons large enough to generate effective exon-specific anti-sense riboprobes (i.e. exon 2 of *mybpc3* and exon 3 of *pln*; Fig. 4A). In a strategy analogous to the splicing-sensitive qPCR, we designed a pair of riboprobes for each gene. One probe detected the total transcript pools of *mybpc3* or *pln*, independent of the alternatively spliced exons ("Total-transcript" in situ hybridization). The other probe detected the alternatively spliced exon sequences exclusively. In control-sibling animals at 33 hpf, total *mybpc3* transcripts were localized to both cardiac and skeletal muscle (Fig. 4D,D'), and total *pln* transcripts were detected exclusively in the heart (Fig. 4H,H'). These expression patterns were unaffected by the loss of *rbpms2* (Fig. 4E,E',I,I'), which is consistent with the total transcript qPCR analysis (Fig. 4B). Isoform-specific in situ hybridization analysis revealed expression of the *rbpms2*-dependent *mybpc3* and *pln* exons exclusively in the hearts of control-sibling animals (Fig. 4F,F',J,J'). Consistent with the isoform-specific qPCR analysis (Fig. 4C), double-mutant animals were completely devoid of these exon sequences (Fig. 4G,G',K,K'). Taken together, these data implicate *rbpms2* as a positive regulator of exon inclusion in the zebrafish embryonic myocardium.

For those alternative splicing events validated by qPCR or in situ hybridization (*mybpc3*, *myom2a*, *pln*, and *slc8a1a*), exon exclusion in mutant hearts maintains the open reading frame, indicating that the hearts of mutant animals express proteins lacking amino acid sequences encoded by the alternatively spliced exons (Fig. 4E,E',G,G'I,I',K,K'). In the case of *mybpc3,* exon 2 encodes a domain termed C0, which is contained exclusively within the cardiac isoform of Myosin Binding Protein C in higher vertebrates (MYBPC3) but is absent from the skeletal muscle isoform [MYBPC2; (McNamara and Sadayappan, 2018)]. Similarly, *mybpc3*'s exon 10

encodes cardiac-specific amino acids that become phosphorylated by protein kinase A (PKA) in response to β-adrenergic signaling (Gautel et al., 1995; Mohamed et al., 1998). For Myom2a, the short stretch of amino acids that disappears in DKO animals is of unknown function. For *pln*, excluding exon 3 shortens the protein by 5 amino acids on the C-terminus, which has been shown to increase SERCA inhibitory activity *in vitro* (Gorski et al., 2015). Lastly, the *slc8a1a* exon with reduced inclusion in DKO animals is one of six conserved exons that are alternatively spliced in higher vertebrates to control the Ca2+ sensitivity of the transporter (Kofuji et al., 1994; Quednau et al., 1997).

Zebrafish rbpms2-null ventricular cardiomyocytes exhibit myofibrillar disarray and calcium handling defects

Because Mybpc3 and Myom2a are sarcomere components, we evaluated 48 hpf control-sibling and double-mutant hearts for myofibrillar defects after immunostaining with antibodies that recognize thin filaments, thick filaments, or Z-disks. For all epitopes, prominent striations were apparent in control-sibling animals reflecting the tandem arrays of sarcomeres composing myofibrils, which themselves are transversely aligned and bundled near the cell cortices (Fig. 5A,A',C-C",E). By contrast, despite the readily-evident detection of epitopes in DKO hearts, striations were significantly reduced or absent because the myofibrils were in a state of disarray (Fig. 5B,B',D-D",F). We confirmed that myofibril disarray was also present in ventricular cardiomyocytes of double mutant animals at an earlier developmental stage of 33 hpf (Fig. S7G-H'). Lastly, this defect is specific to ventricular cardiomyocytes because myofibril organization in atrial cardiomyocytes of control and DKO embryos was grossly indistinguishable (Fig. S7I-J'). Taken together, these data demonstrate that Rbpms2 activity is required for establishing or maintaining the three-dimensional architecture of myofibrils in ventricular cardiomyocytes of the zebrafish embryo.

Lastly, because *pln* and *slc8a1a* regulate calcium handing in cardiomyocytes (Koushik et al., 2001; Langenbacher et al., 2005; Simmerman and Jones, 1998; Toyoshima et al., 2003), we evaluated *rbpms2*-null hearts for abnormalities in the amplitude or duration of cytosolic calcium transients, which stimulate cardiomyocyte contraction. To that end, control-sibling and *rbpms2*-null hearts at 48 hpf were explanted and loaded with the dual-wavelength calcium-sensitive dye Fura-2. High-speed imaging was performed to obtain a ratiometric indicator of fluctuating calcium in cardiomyocytes over several cardiac cycles (Russell, 2011). From this, we measured the duration and amplitude of the calcium transients in the atrium and ventricle of control-sibling and *rbpms2*-null hearts. Whereas these values were not significantly different in the atrium of double mutant hearts (Fig. 6A,B,D-F,H), both the duration and amplitude of the calcium transients in double mutant ventricles were reduced in the mutant ventricle (Fig. 6A-C; E-G), demonstrating that Rbpms2 is indispensable for the regulation of calcium handling in ventricular cardiomyocytes of the zebrafish embryo.

Human RBPMS2-null cardiomyocytes exhibit myofibrillar disarray and calcium handling defects

To determine if the cellular function of *RBPMS2* is conserved in human cardiomyocytes, we targeted *RBPMS2* in human induced pluripotent stem cells (hiPSCs) using CRISPR/Cas9-mediated genome editing and analyzed phenotypes that arose following differentiation into hiPSC-derived cardiomyocytes (hiPSC-CMs). We targeted the DNA sequence encoding RBPMS2's RNA recognition motif and isolated a clone with a biallelic 2 base-pair deletion (Fig. S10A; *ΔRBPMS*), which truncates both the protein and the RRM by ~70% due to a premature stop codon (Fig. 7A; Fig. S10B). Quantitative RT-PCR analysis revealed a significant 82% reduction in *RBPMS2* transcripts in *ΔRBPMS* hiPSCs (Fig. 7B) and hiPSC-CMs (Fig. 7C), suggesting that the mutant transcripts are susceptible to non-sense mediated decay. This

observation, in combination with the large size of the C-terminal truncation (Fig. 7A) strongly suggest that *ΔRBPMS2* cells are null for *RBPMS2*.

To determine if *RBPMS2*-null human cardiomyocytes exhibit cellular phenotypes similar to those observed in ventricular cardiomyocytes from *rbpms2*-null zebrafish (Fig. 5A-F), we analyzed myofibril structure in control-parental and *ΔRBPMS2* hiPSC-CMs by double immunostaining with antibodies that detect thin filaments or Z-disks. The hallmark striations created by thin filaments, which were readily apparent in control cells (Fig. 7D,E,G), were almost completely absent in *ΔRBPMS2* hiPSC-CMs (Fig. 7H,I,K). Moreover, whereas the Z-disks in control cardiomyocytes were prominent, well defined and arrayed in parallel (Fig. 7D,F,G), those in *ΔRBPMS2* hiPSC-CMs were smaller, punctate, and disorganized (Fig. 7H,J,K). Taken together, these data uncover a conserved role for RBPMS2 in establishing or maintaining myofibril organization in human cardiomyocytes.

Lastly, we evaluated control-parental and *ΔRBPMS2* hiPSC-CMs for defects in calcium handling. hiPSC-CMs cells were loaded with the calcium-sensitive dye Fluo-4, paced at 1Hz and imaged by line scanning confocal microscopy to capture intracellular Ca2+ dynamics (Fig. 7L,M). Similar to ventricular cardiomyocytes from *rbpms2*-null zebrafish, *ΔRBPMS2* hiPSC-CMs exhibited significant decreases in Ca2+-transient amplitude (Fig. 7N) and transient duration (Fig. 7O,P). These phenotypes were accompanied by decreases in time-to-peak (Fig. 7Q) and maximum upstroke velocity (Fig. 7R). Lastly, without pacing, *ΔRBPMS2* hiPSC-CMs contracted at a lower spontaneous beat frequency (Fig. 7S). These data demonstrate that human cardiomyocytes rely on RBPMS2 function for optimal calcium handling. Taken together, the overlap in sarcomere and calcium handling phenotypes observed between *Rbpms2*-null zebrafish and *ΔRBPMS2* hiPSC-CMs suggest that the cellular function(s) of this myocardial RNA-binding protein is conserved in human cardiomyocytes.

DISCUSSION

Our study identifies Rbpms2 proteins as critical RNA splicing factors that regulate tissue-specific isoform expression within the ventricular myocardium. Specifically, we show that zebrafish Rbpms2a and Rbpms2b are redundantly required for ventricular form and function in embryonic zebrafish. We then show that Rbpms2 proteins function to promote the generation of distinct isoforms within the heart, including a previously undocumented cardiac-specific isoform of *mybpc3*. Further, we found that *rbpms2*-null hearts have disorganized sarcomeres and disrupted calcium handling, which is phenotypically consistent with the broad classes of alternatively spliced transcripts identified by our RNA-seq. Lastly, we discovered that RBPMS2-deficient human iPSC-CMs exhibit defects in sarcomere structure and calcium handling that are strikingly similar to what we observed in zebrafish ventricles.

Our characterization of Rbpms2 provides further evidence that RNA splicing within the heart may be a much more pervasive and physiologically important mode of gene regulation than previously appreciated. While our results reveal a clear connection between Rbpms2 and RNA splicing, these proteins may function in additional capacities within tissues outside the heart. Previous reports in zebrafish have shown that Rbpms2 proteins contribute to the establishment of oocyte polarity and development by influencing the localization of RNAs such as *bucky ball* (*buc*) to the Balbiani body(Heim et al., 2014; Kaufman et al., 2018; Kosaka et al., 2007). Further research in xenopus and chicken have described similar roles for Rbpms2 in RNA stability and localization within intestinal smooth muscle, kidney cells, and retinal ganglion cells(Farazi et al., 2014; Hörnberg et al., 2013; Notarnicola et al., 2012). Interestingly, the localization of Rbpms2 to stress granules has been observed in several of these models(Farazi et al., 2014; Furukawa et al., 2015), indicating that this function may be conserved in multiple tissues. It will be important to determine if RBPMS2 functions in this capacity within the heart, or whether this is a tissue-specific function that is restricted to other RBPMS2-positive organs such as the eye and nephron.

Even though we found that Rbpms2 regulates the splicing of genes whose orthologs are known to cause cardiomyopathy, it is unclear whether mutations in RBPMS2 segregate with human disease. Our data therefore warrants a careful re-evaluation of existing GWAS datasets and provides new incentives to examine the RBPMS2 locus in CHD patients. However, given the severity of cardiac phenotypes observed in our loss-of-function experiments, it remains possible that embryonic lethality may confound GWAS results. Additionally, the upstream regulators of Rbpms2 remain unknown. Further studies will be necessary to identify these upstream factors in order to determine if they contribute to disease states through a more subtle modulation of Rbpms2 function. Given that Rbpms2 is itself alternatively spliced in vertebrates, it is also possible that its function may be regulated by yet another upstream splicing factor. Collectively these studies will evaluate RBPMS2 function within the broader context of human cardiomyopathy and heart failure.

METHODS

Zebrafish husbandry and strains

Zebrafish were bred and maintained following animal protocols approved by the Institutional Animal Care and Use Committees at Massachusetts General Hospital and Boston Children's Hospital. All protocols and procedures followed the guidelines and recommendations outlined by the Guide for the Care and Use of Laboratory Animals. The following zebrafish strains were used in this study: *TgBAC(-36nkx2.5:ZsYellow)*^{fb7} (Zhou et al., 2011), *Tg(myl7:GFP)*^{fb1} [formerly *Tg(cmlc2:GFP)*^{fb1}*]* (Burns et al., 2005)*, Tg(myl7:NLS-eGFP)*^{fb18} [formerly *Tg(cmlc2:nucGFP)*^{fb18}*]* (González-Rosa et al., 2018)*, Tg(myl7:actn3b-EGFP)*^{sd10} [formerly *Tg(cmlc2:actinin3-EGFP)]* (Lin et al., 2012)*, rbpms2a*^{chb3} (this study), and *rbpms2b*^{chb4} (this study).

Sample preparation for RNA-sequencing and differential expression analysis

Tg(nkx2.5:ZsYellow) embryos at the 14-16 somites stage were dechorionated with pronase and washed several times with excess E3 medium. Approximately 1,200 embryos were transferred to a 1.5ml Eppendorf tube, centrifuged at low speed, and washed three times with 0.9X PBS. Embryos were suspended in 750μl of ice-cold 0.9X PBS plus 5% FBS (PBS/FBS) and homogenized with a disposable plastic pestle before being drawn up-and-down multiple times into a p1000 micropipette. The cells were passed over a 40μm nylon cell strainer and collected in a pre-chilled 50ml Falcon tube on ice. The strainer was subsequently rinsed with 25ml of ice-cold PBS/FBS and the flowthrough was collected in the same Falcon tube. Cells were pelleted by low-speed centrifugation for 5 minutes at 4°C. The majority of supernatant was removed with a Pasteur pipette and the pellet was resuspended in 2ml of ice-cold PBS/FBS. Cells were passed over another 40μm strainer, collected in a pre-chilled 15ml Falcon tube and pelleted by low-speed centrifugation for 5 minutes at 4°C. Cells were resuspended in approximately 1ml ice-cold PBS/FBS and stored on ice. Fluorescence activated cell sorting was used to separate ZsYellow-positive from ZsYellow-negative cells. Both subpopulations were collected independently and frozen. From each sort, averages of 39K ZsYellow-positive cells (range 23-68K) and 50K ZsYellow-negatieve cells were collected. Total RNA was purified using the RNeasy Kit (Qiagen Sciences Inc). Material from either 4 (ZsYellow-positive) or 5 (ZsYellow-negative) sorts was combined to generate single replicates. Two replicates per experimental group, consisting of RNA purified from 147K or 166K total ZsYellow-positive cells and 250K total ZsYellow-negative cells, were included in the RNA-sequencing and differential expression analysis. Control-sibling and *rbpms2*-null embryos at 33 hpf were separated based on morphology and collected into pools (10 animals per pool). Pools were mechanically homogenized by vigorous pipetting in 500μl TRIzol Reagent (Thermo Fisher Scientific). For each pool, a 200μl sample of the homogenization solution was removed and phase-separated to obtain DNA for confirmatory genotyping. The remaining 300μl was processed via Direct-zol

RNA MicroPrep columns (Zymo Research) to obtain total RNA for one biological replicate. Five biological replicates for each experimental group were included in the RNA-sequencing and differential expression analysis.

Tg(nkx2.5:ZsYellow) FACS RNA-Seq strategy and analysis

RNA sample quality was evaluated using a 2100 Bioanalyzer Instrument (Agilent Technologies). Approximately 50ng of RNA per sample were used to prepare sequencing libraries with the Clontech low-input RNA library preparation kit. Libraries were sequenced as paired-end 2x50nt on an Illumina HiSeq2500 instrument. Quality control was performed by aligning reads against Zv9/danRer7 using bwa mem v. 0.7.12-r1039 with flags –t 16 –f and mapping rates, fraction of multiply-mapping reads, number of unique 20-mers at the 5' end of the reads, insert size distributions and fraction of ribosomal RNAs were calculated using dedicated perl scripts and bedtools v. 2.25.0.64 (Quinlan and Hall, 2010). In addition, each resulting bam file was randomly down-sampled to a million reads, which were aligned against Zv9/danRer7 and read densities across genomic features were estimated for RNA-Seq-specific quality control metrics. Read mapping and quantification was performed using Salmon v. 1.2.1 (Patro et al., 2017), with the following flags: quant -l IU --validateMappings in paired-end mode against the GRCz11/danRer11 genome assembly and ENSEMBL 100 annotation, using all GRCz11 sequences as decoys. Quantification files were processed in R using the txImport function and per-gene counts and TPM estimates were retrieved (Soneson et al., 2016).

rbpms2-null RNA-Seq strategy and analysis

RNA integrity and concentration were checked on a Fragment Analyzer (Advanced Analytical) and libraries were prepared using the Illumina NeoPrep RNAseq kit. Blue Pippin size selection was performed, selecting for 350 nt fragments. Libraries were quantified using the Fragment Analyzer (Advanced Analytical) and qPCR before being loaded for paired-end sequencing 2x75

nucleotides using the Illumina NextSeq 500 in High Output mode. For quality control purposes, reads were aligned against GRCz10/danRer10 (Sept. 2014) using bwa mem v. 0.7.12-r1039 with flags –t 16 –f and mapping rates, fraction of multiply-mapping reads, number of unique 20-mers at the 5' end of the reads, insert size distributions and fraction of ribosomal RNAs were calculated using dedicated perl scripts and bedtools v. 2.25.0.64 (Quinlan and Hall, 2010). In addition, each resulting bam file was randomly down-sampled to a million reads, which were aligned against GRCz10/danRer10 and read density across genomic features were estimated for RNA-Seq-specific quality control metrics. RNA-Seq mapping and quantitation was done against GRCz10 / ENSEMBL 89 annotation using STAR v. 2.5.3a (Dobin et al., 2013) with flags -runThreadN 8 --runMode alignReads --outFilterType BySJout --outFilterMultimapNmax 20 --alignSJoverhangMin 8 --alignSJDBoverhangMin 1 --outFilterMismatchNmax 999 --alignIntronMin 10 --alignIntronMax 1000000 --alignMatesGapMax 1000000 --outSAMtype BAM SortedByCoordinate --quantMode TranscriptomeSAM with --genomeDir pointing to a 75nt-junction GRCz10/danRer10 STAR suffix array. Gene expression was quantitated using RSEM v. 1.3.0 (Li and Dewey, 2011) with the following flags for all libraries: rsem-calculate-expression --calc-pme --alignments -p 8 --forward-prob 0 against an annotation matching the STAR SA reference. Posterior mean estimates (pme) of counts and estimated RPKM were retrieved. For both RNA-Seq experiments, differential expression analysis was performed using DESeq2 on count data comparing Nkx2.5+ vs. bulk and *rbpms2*-null vs. wild-type samples, respectively. For *rbpms2*-null analyses, a batch correction was introduced in the form of a count ~ genotype+batch additive model, given substantial batch-related sample dispersion upon visual inspection of the first and second principal components of variance. No Cook's cutoff, independent filtering nor log-fold-change shrinkage were applied. Log2-fold changes as well as raw and Benjamini-Hochberg adjusted p-values were calculated for each protein-coding gene (Love et al., 2014).

Splicing analysis

Analysis of differential RNA processing in *rbpms2*-null vs. WT samples was performed in three distinct ways. Initially, isoform-level expression data were retrieved from RSEM and analyzed in DESeq2, using the posterior mean estimates of the counts per isoform as input and a similar batch-correction strategy as the gene-level differential-expression analysis described above. Additionally, the dedicated splicing analysis algorithm rMATS.3.2.5 was run on the data as RNASeq-MATS.py with flags - -t paired -len 75 -c 0.1 -analysis U -libType fr-firststrand -novelSS 1 -keepTemp pointing to the same GTF file and STAR index used at the read mapping star, across all samples and batches. Event inclusion was quantified both by counting junction reads only and junction and read on targets. The resulting data collated across replicates were filtered, and events had to meet the following conditions to be retained: the event had to be called in all samples, differences in inclusion levels had to be > 0.1 or < -0.1 and false-discovery rate < 0.1. Finally, the MISO algorithm was used to assess expression and usage of complex alternative isoforms of the pln gene and visualized with Sashimi plots (Katz et al., 2010, 2015). Briefly, dedicated annotations of the isoforms of interest were generated manually and run using MISO v. 0.5.3 in the python 2.7 environment with default parameters and --read-len 75. MISO outputs were compared between genotypes within each batch using the compare_miso –compare-samples function.

Generation and genotyping of *rbpms2a*^{ch3} and rbpms2*b*^{ch4} mutant alleles

Customized transcription activator-like effector nucleases (TALENs) (Ma et al., 2013; Sander et al., 2011; Sanjana et al., 2012) were used to induce double-stranded breaks in regions of the *rbpms2a* and *rbpms2b* loci that encode the RNA-recognition motifs. TALENs were designed to bind the sequences 5'- TGCCTGTTGACATCAAGC-3' (+) and 5'-TTGAAGGGTCTGAACAGC-3' (-) in exon 2 of *rbpms2a* and 5'- TGCCAACAGATATCAAAC-3' (+) and 5'-TTAAATGGTCGAAATAGC-3' (-) in exon 2 of *rbpms2b*. TALEN constructs were constructed as

described (Sanjana et al., 2012). Messenger RNAs encoding each TALEN pair were produced in vitro and co-injected into one-cell stage zebrafish embryos as described (Ma et al., 2013) Germline transmission of TALEN-induced mutations was detected using fluorescent PCR and DNA-fragment analysis as described (Foley et al., 2009). The nucleotides deleted in the mutant alleles *rbpms2a*^{chb3} and *rbpms2b*^{chb4} are shown (Fig. S4A,B). The primers utilized to distinguish wild-type *rbpms2a* and *rbpms2b* from the mutant alleles *rbpms2a*^{chb3} and *rbpms2b*^{chb4} by fluorescent PCR and DNA-fragment analysis are shown (Table S5). The wild-type alleles produce amplicons of 97 base pairs (bp)(*rbpms2a*) and 76bp (*rbpms2b*), whereas the mutant alleles produce amplicons of 83bp (*rbpms2a*^{chb3}) and 74bp (*rbpms2b*^{chb4}).

Whole mount in situ hybridization

In situ hybridization was performed essentially as described (Thisse and Thisse, 2008). Templates for generating anti-sense riboprobes for *rbpms2a, rbpms2b, mybpc3* isoform-specific*, mybpc3* total transcript*, pln* isoform-specific*,* and *pln* total transcript targets were generated by PCR or by gBlock (IDT) using the respective primer pairs or gBlock sequences shown in Table S6. All sequences were cloned into pCR4 vector using the TOPO TA cloning kit (Thermo Fisher Scientific). The *rbpms2a* and *rbpms2b* templates were linearized with BamHI and KpnI respectively, and Digoxygenin-labeled antisense probes were generated using T7 polymerase. Templates for *pln* isoform-specific, *pln* total transcript, and *mybpc3* total transcript probes were linearized with SpeI and transcribed using T7. The template for the *mybpc3* isoform-specific probe was linearized with NotI and transcribed with T3 polymerase. All probes were synthesized using the DIG RNA Labeling Kit (SP6/T7/T3; Millipore Sigma) and colorimetric reactions were performed using the NBT/BCIP chromogenic substrate (Promega Corp.).

Whole mount immunofluorescence and confocal imaging

Embryos were treated with 0.5M KCl to arrest hearts in diastole prior to fixation overnight in phosphate-buffered saline (PBS) containing 4% paraformaldehyde (PFA). The following day, embryos were thoroughly washed with PBS and dehydrated through a methanol series for storage at -20°C. Prior to staining, embryos were rehydrated into PBS containing 0.1% Tween-20 (PBST) and treated with bleaching solution (0.8% KOH, 0.9% H_20_2, 0.1% Tween-20) to remove pigment. Embryos were washed with PBST and permeabilized for 1 hour in PBS containing 0.5% Triton X-100. Prior to antibody incubation, embryos were blocked in 5% bovine serum albumin (BSA) and 5% goat serum in PBST for 1 hour. Embryos were incubated with primary antibodies diluted in blocking solution overnight at 4°C. The following primary antibodies were utilized: anti-Troponin T (CT3; Developmental Studies Hybridoma Bank (DSHB); 1:500 dilution), anti-GFP (B-2; Santa Cruz Biotechnology; 1:100), anti-RBPMS2 (ab181098; abcam; 1:500), anti-Tropomyosin (CH1; DSHB; 1:200) and anti-Myosin heavy chain (MF20; DSHB; 1:50). Embryos were washed in PBST and incubated with Alexa Fluor-conjugated secondary antibodies listed in the STAR methods table (1:500, Thermo Fisher Scientific) for 1-3 hours at room temperature. Following incubation, embryos were washed in PBST and nuclei labeled with DAPI for 5' (Sigma-Aldrich; 1:5000). Embryo heads were then removed to expose the heart. Embryos were mounted in 0.9% low-melt agarose on glass-bottom dishes (MatTek Corp.) for imaging on a Nikon Ti Eclipse confocal microscope. Images were processed and/or analyzed for nuclei counts with ImageJ (Schneider et al., 2012) Further processing was performed in Photoshop (Adobe Inc.).

Western Blotting

Western blotting was performed as previously described (Jahangiri et al., 2016). Lysates were prepared from pools of 5 embryos at 48 hpf and were probed with anti-RBPMS2 (ab181098; abcam; 1:1000) and anti-Alpha Tubulin (DM1A; Millipore; 1:10,000) overnight at 4°C. HRP-

conjugated anti-rabbit (7074; Cell Signaling) and anti-mouse (7076; Cell Signaling) secondary antibodies were used at a 1:10,000 dilution.

Histological sectioning and staining

Paraffin sections of adult zebrafish hearts were generated following conventional procedures used for dissected mouse hearts. Briefly, hearts were dissected and fixed overnight in 4% PFA followed by washes in PBS and serial dehydration into 100% ethanol. Hearts were stored in 100% ethanol overnight at 4°C to and cleared with xylenes prior to paraffin embedding. 7μm sections were then transferred to microscope slides for histological or antibody staining. Prior to staining, slides were taken back through xylenes, 100% ethanol, and into water or PBS. Hematoxylin and Eosin (H&E) staining of paraffin sections were performed using conventional methodology and reagents (Sigma-Aldrich). Acid fuchsin/Orange G (AFOG) staining was performed as previously described (Poss et al., 2002) using Bouins solution (Thermo Fisher Scientific), aniline blue (Sigma-Aldrich), orange G (Sigma-Aldrich), and acid fuchsin (Sigma-Aldrich). H&E or AFOG stained sections were dehydrated in ethanol, washed with xylenes, and mounted with Cytoseal (Thermo Fisher Scientific) prior to imaging. Immunostaining of paraffin sections was performed as previously described (Akerberg et al., 2017) using anti-RBPMS2 (ab181098; abcam; 1:500) and anti-Myosin heavy chain (MF20; DSHB; 1:50) antibodies followed by incubation with DAPI for 5' (Sigma-Aldrich; 1:5000). Stained sections were then mounted with Fluorsave (Millipore) and kept in the dark.

Assessments of cardiac function

Volumetric measurements of the zebrafish heart were performed at ~48 hpf using light sheet fluorescence microscopy and the deep-learning neural network CFIN as described previously (Akerberg et al., 2019b). Briefly, live-mounted *Tg(myl7:GFP*) zebrafish were imaged with a 60X

objective on a custom light sheet fluorescence microscope that was built based on a previously published design (Huisken and Stainier, 2007; Power and Huisken, 2017). Hearts were imaged through the entire ventricle by collecting dynamic plane images at each GPF-positive z depth. Dynamic images were taken every 1µm and spanned at least four cardiac cycles. In order to ensure optimal CFIN performance with images acquired on a custom-built microscope, a subset of these images were manually labeled and used to retrain the network as previously described. Experimental images were then processed and analyzed by CFIN in MATLAB (MathWorks). Fractional shortening (FS) in 33 hpf hearts was determined from videos of *Tg(myl7:GFP*) zebrafish hearts. One-dimensional measurements of the arterial pole width during diastole (d) and systole (s) were obtained in ImageJ and used to calculate percent FS.

Reverse transcription quantitative polymerase chain reaction (RT-qPCR)

Total RNA was harvested from pooled material (10 embryos or 10 dissected hearts per pool) using TRIzol reagent and purified via Direct-zol RNA MicroPrep columns (ZYMO). cDNA synthesis was performed using Superscript III (Invitrogen). RT-qPCR was performed on the QuantStudio 3 Real-Time PCR system (Applied Biosystems) using KAPA SYBR FAST qPCR master mix reagents (Kapa Biosystems). Relative mRNA expression was determined after normalizing to *rps11* using the ΔΔCt method (Livak and Schmittgen, 2001). 3 biological replicates (3 separate pools of 10 embryos each) and 3 technical replicates were performed for each experiment. Statistical significance was determined by an unpaired, two-tailed Student's t-test assuming equal variances.

RNA immunoprecipitation (RIP)

Adult zebrafish hearts (fish > 2 months old) were harvested, pooled (2 pools of 20 hearts/pool) and dissociated into a single cell suspension as previously described (González-Rosa et al., 2018). Cell suspensions were spread into a thin layer and irradiated with 254 nm light at 200mj

per cm^2 to cross link. Nuclei were then isolated using the NE-PER nuclear and cytoplasmic extraction kit (Thermo Fisher Scientific), spun down, and flash frozen in liquid nitrogen. RIPs were performed as previously described (Minajigi et al., 2015) using magnetic beads bound with either rabbit anti-Rbpms2 or negative control rabbit IgG antibodies. Following the RIP, beads were resuspended in 20µg proteinase K and incubated for 1 hour at 55ºC. RNA was then isolated by resuspension in TRIzol (Thermo Fisher Scientific) and Direct-zol RNA purification (Zymo Research). RNA from each pool and their corresponding Inputs were sequenced and used to determine enrichment.

Calcium imaging of zebrafish hearts

Hearts were isolated manually from 48 hpf zebrafish embryos and placed in normal Tyrode's (NT) solution [NT contains 136mM NaCl, 5.4mM KCl, 1mM $MgCl_2x6H_2O$, 5mM D-(+)-Glucose, 10mM HEPES, 0.3mM $Na_2HPO_4x2\ H_2O$, 1.0mM $CaCl_2x2\ H_2O$, pH 7.4] supplemented with 8 mg/ml BSA. For ratiometric Ca2+-transient recordings, hearts were loaded for 15 minutes with 50µM of the Ca2+-sensitive dye Fura-2, AM (Thermo Fisher Scientific) and subsequently incubated in due-free NT buffer with BSA for 45' to allow complete intracellular hydrolysis of the esterified dye. Individual hearts were loaded into a perfusion chamber (RC-49MFS, Warner Instruments) mounted on an inverted microscope (TW-2000, Nikon). The perfusion chamber contained NT supplemented with 1mM Cytochalasin D to inhibit cardiac contraction. A high-speed monochromator (Optoscan, Cairn Research) was used to rapidly switch the excitation wavelength between 340nm and 380nm with a bandwidth of 20nm and at a frequency of $500s^{-1}$. The excitation light, generated by a 120W metal halide lamp (Exfo X-Cite 120, Excelitas Technologies) was reflected by a 400nm cutoff dichroic mirror and fluorescence emission was collected by the camera through a 510/580nm emission filter. For the measurement of fluorescence intensities, we used a high-speed 80×80-pixel CCD camera (CardioCCD-SMQ, RedShirtImaging, LLC) with 14-bit resolution. For ratiometric Ca2+-transient recordings,

monochromator and camera were synchronized. Because each wavelength change required a mechanical movement of the grating, each ratio required the recording of four frames, where one frame was used for each transition between wavelengths. This ultimately resulted in the acquisition of ratiomateric Ca2+ measurements at a frequency of 125 Hz. Measurements were performed using a 40x objective and a 0.28x C-mount adapter (final magnification was 11.2x), resulting in a pixel-to-pixel distance of 2.14µm. Images were analyzed and Ca2+ transient durations, amplitudes and diastolic Ca2+ were quantified with MATLAB (Mathworks) using customized software as previously described (Panáková et al., 2010). The values plotted in Fig. 6 represent recordings from the center of each chamber.

hiPSC maintenance and genome editing

All hiPSC lines were maintained at 37°C, 5% CO_2 in Essential 8 medium (Cat. # A1517001, Thermo Fisher Scientific) and passaged every 3 – 4 days using Versene (Cat. # 15040066, Thermo Fisher Scientific). Culture dishes were pre-coated with 0.5% GelTrex matrix solution (Cat. # A1413302, Thermo Fisher Scientific). CRISPR/Cas9 genome editing was performed to create isogenic lines. Briefly, guide RNA for *RBPMS2* (sequence 5'-GTCTTGCAGTGAGCTTGATC-3') was synthesized using the T7 MegaShortScript transcription kit (Thermo Fisher Scientific). We previously described methods (Wang et al., 2017) to generate a doxycycline -inducible Cas9 line in the WTC-11 iPSC background (Coriell Institute). Targeted integration of Cas9 into the AAVS1 locus was performed using Addgene plasmids #73500 and #48139. This WTC-11 AAVS1$^{Cas9/+}$ hiPSC line was treated with doxycycline (2µg/ml) for 16 hours prior to transfection to induce expression of an NLS-SpCas9 fusion protein. After induction, approximately 0.5 x10^6 cells were transfected with 10µg guide RNA using an Amaxa nucleofector (Lonza Technologies). Cells were seeded at a low density to pick single clones. Positive clones were confirmed by Sanger and amplicon sequencing. Stem cell marker

expression was validated in isolated cell lines by flow cytometry using anti-SSEA4-FITC (Cat. # 130-098-371, Miltenyi Biotec).

Cardiomyocyte Differentiation

hiPSC were seeded onto 12-well plates at 60,000 cells/well and maintained for 48 hours prior to differentiation or until they reached 60% confluence. On days 0 – 2 of differentiation, cells were cultured with RPMI (Cat. # 11875093, Thermo Fisher Scientific) supplemented with B27 minus insulin (Cat. # A1895601, Thermo Fisher Scientific) and 6µM CHIR99021 (Cat. # 72054, Stem Cell Technologies). Cells were replenished with RPMI/B27(-insulin) on day 3, then cultured with RPMI/B27(-insulin) supplemented with 5µM IWR1-endo (Cat. # 2564, Stem Cell Technologies) on days 4 and 5. From days 6 – 12, cells were maintained in RPMI/B27(-insulin) with media changes every 48 hours. Lactate selection was performed on day 12 for 48hrs with RPMI supplemented with 5mM sodium lactate (Cat. # L7022, MilliporeSigma). For downstream experiments, iPSC-CMs were dissociated using StemPro Accutase (Cat. A1110501, Thermo Fisher Scientific). Cells were gently resuspended with an equal volume of RPMI/B27 supplemented with 5% FBS and 5µm ROCK inhibitor (Y-27632, Tocris), passed through a 70µm cell strainer and pelleted at 200 x g for 5 min.

Immunostaining for hiPSC-CMs

hiPSC-CMs were dissociated as stated above and re-plated on glass cover slips coated in GelTrex. Cells were allowed to recover in RPMI/B27 with 5% FBS and 5µm ROCK inhibitor overnight followed by replacement with RPMI/B27 every 48 hours until fixation. Cells were fixed in 4% PFA (10 minutes) and permeabilized in PBS with 0.1% Triton X-100 (5 minutes). Cells were blocked in PBS with 3% BSA and incubated with primary antibodies overnight at 4°C. The following primary antibodies were utilized: anti-Sarcomeric alpha actinin (ab9465; abcam; 1:500)

and anti-Troponin T (CT3; DSHB; 1:500) followed by DAPI staining to mark nuclei. Stained coverslips were mounted with FluorSave (Millipore) and stored in the dark.

Calcium imaging of hiPSC-CMs

Single line scanning confocal microscopy was used to record calcium transients and calcium release events. In brief, 100,000 hiPSC-CMs were seeded onto 8mm GelTrex-coated coverslips and cultured for 4 days. Cells were loaded with 1uM fluo-4 calcium indicator (Cat. F14201; Thermo Fisher Scientific) prepared in Tyrode's solution [137mM NaCl, 2.7mM KCl, 1mM $MgCl_2$, 1.8mM $CaCl_2$, 0.2mm Na_2-HPO_4, 12mM $NaHCO_3$, 5.5mM D-Glucose, pH7.4] for 10 minutes at 37°C. Cells were then washed with DPBS and incubated in Tyrode's solution for 10 minutes prior to imaging. Temperature-controlled calcium measurements were acquired for a total duration of 30s using the following imaging protocol: 10s spontaneous recording, 10s paced, 10s recovery. Cells were electrically paced at 1hz with 15V using a MyoPacer (IonOptix). Multiple line scans were compiled in Image J (Schneider et al., 2012) using a custom macro. Calcium transient kinetics were analyzed using a homemade MATLAB (MathWorks) script.

Data Availability

RNA-sequencing datasets were deposited into the NCBI GEO repository under accession numbers GSE167416 and GSE167414.

ACKNOWLEDGEMENTS

Fluorescence activated cell sorting was performed at the Harvard Stem Cell Institute-Center for Regenerative Medicine Flow Cytometry Core. Customized TALENs were generated by the Broad Institute Genetic Perturbation Platform (Director: John Doench, PhD). Library preparation and RNA-sequencing were performed at the MIT BioMicroCenter (Director: Stuart Levine, PhD).

Sanger sequencing and DNA fragment analysis were performed at the Massachusetts General Hospital Computational and Integrative Biology DNA Core (Director: Amy Avery).

FUNDING

AAA and AS were supported by a National Institutes of Health (NIH) training grant awarded to MGH (T32HL007208; PI: A. Rosenzweig). AAA was supported by an American Heart Association Postdoctoral Fellowship (20POST35110027). The Burns Laboratory was supported by NIH grants 7R01HL139806 (formerly 1R01HL139806) and 7R35HL135831 (formerly 1R35H135831) to CGB and CEB, respectively, by awards from the Executive Committee on Research at Massachusetts General Hospital (MGH) to CGB, and by Department of Defense Peer-Reviewed Medical Research Program (PRMRP) grant PR190628 to CEB. CEB was a d'Arbelhoff MGH Research Scholar. CGB was a Hassenfeld Cardiovascular Scholar at MGH. The Burns Laboratory was supported, in part, by funds from the Boston Children's Hospital Department of Cardiology.

AUTHOR CONTRIBUTIONS

AAA designed, performed, and interpreted the majority of experiments. MT provided guidance on hiPSC handling, mutant isolation, cardiomyocyte differentiation, and immunostaining. He also performed calcium imaging on hiPSC-CMs. VB performed bioinformatics analysis. AS sorted ZsYellow-positive and ZsYellow-negative cells from *Tg(nkx2.5:ZsYellow)* embryos, harvested RNA from sorted cells, isolated the *rbpms2a*^{ch3} and *rbpms2b*^{ch4} alleles, performed western blotting, contributed to in situ hybridization analysis of *rbpms2a/b*, and aided AAA with CM counts. LZ cloned *rbpms2a* and *rbpms2b* riboprobe templates. XJ constructed the WTC-11$^{Cas9/+}$ iPSC line. MB performed calcium imaging in zebrafish. MSS and SY assisted with light sheet imaging. CN assisted with CFIN programming and analysis. CM and WP acquired funding

and provided guidance. CEB and CGB directed the study, designed experiments, and interpreted data. AAA, CEB, and CGB wrote the manuscript with input from all authors.

COMPETING INTERESTS

The authors declare no competing interests.

References

Agarkova, I., and Perriard, J.-C. (2005). The M-band: an elastic web that crosslinks thick filaments in the center of the sarcomere. Trends Cell Biol *15*, 477–485.

Akerberg, A.A., Henner, A., Stewart, S., and Stankunas, K. (2017). Histone demethylases Kdm6ba and Kdm6bb redundantly promote cardiomyocyte proliferation during zebrafish heart ventricle maturation. Dev Biol *426*, 84–96.

Akerberg, A.A., Burns, C.E., and Burns, C.G. (2019a). Exploring the Activities of RBPMS Proteins in Myocardial Biology. Pediatric Cardiology *40*, 1410–1418.

Akerberg, A.A., Burns, C.E., Burns, C.G., and Nguyen, C. (2019b). Deep learning enables automated volumetric assessments of cardiac function in zebrafish. Disease Models & Mechanisms *12*, dmm040188.

Berdougo, E., Coleman, H., Lee, D.H., Stainier, D.Y.R., and Yelon, D. (2003). Mutation of weak atrium/atrial myosin heavy chain disrupts atrial function and influences ventricular morphogenesis in zebrafish. Development (Cambridge, England) *130*, 6121–6129.

Biesiadecki, B.J., Elder, B.D., Yu, Z.-B., and Jin, J.-P. (2002). Cardiac Troponin T Variants Produced by Aberrant Splicing of Multiple Exons in Animals with High Instances of Dilated Cardiomyopathy*. J Biol Chem *277*, 50275–50285.

Burns, C.G., Milan, D.J., Grande, E.J., Rottbauer, W., MacRae, C.A., and Fishman, M.C. (2005). High-throughput assay for small molecules that modulate zebrafish embryonic heart rate. Nat Chem Biol *1*, 263–264.

Cuspidi, C., Negri, F., Sala, C., Valerio, C., and Mancia, G. (2011). Association of left atrial enlargement with left ventricular hypertrophy and diastolic dysfunction: A tissue Doppler study in echocardiographic practice. Blood Pressure *21*, 24–30.

Cuspidi, C., Rescaldani, M., and Sala, C. (2013). Prevalence of Echocardiographic Left-Atrial Enlargement in Hypertension: A Systematic Review of Recent Clinical Studies. Am J Hypertens *26*, 456–464.

Dobin, A., Davis, C.A., Schlesinger, F., Drenkow, J., Zaleski, C., Jha, S., Batut, P., Chaisson, M., and Gingeras, T.R. (2013). STAR: ultrafast universal RNA-seq aligner. Bioinformatics *29*, 15–21.

Ebert, A.M., Hume, G.L., Warren, K.S., Cook, N.P., Burns, C.G., Mohideen, M.A., Siegal, G., Yelon, D., Fishman, M.C., and Garrity, D.M. (2005). Calcium extrusion is critical for cardiac morphogenesis and rhythm in embryonic zebrafish hearts. Proceedings of the National Academy of Sciences of the United States of America *102*, 17705–17710.

Farazi, T.A., Leonhardt, C.S., Mukherjee, N., Mihailovic, A., Li, S., Max, K.E.A., Meyer, C., Yamaji, M., Cekan, P., Jacobs, N.C., et al. (2014). Identification of the RNA recognition element of the RBPMS family of RNA-binding proteins and their transcriptome-wide mRNA targets. RNA (New York, N.Y.) *20*, 1090–1102.

Farza, H., Townsend, P.J., Carrier, L., Barton, P.J., Mesnard, L., Bährend, E., Forissier, J.-F., Fiszman, M., Yacoub, M.H., and Schwartz, K. (1998). Genomic Organisation, Alternative Splicing and Polymorphisms of the Human Cardiac Troponin T Gene. J Mol Cell Cardiol *30*, 1247–1253.

Foley, J.E., Yeh, J.-R.J., Maeder, M.L., Reyon, D., Sander, J.D., Peterson, R.T., and Joung, J.K. (2009). Rapid Mutation of Endogenous Zebrafish Genes Using Zinc Finger Nucleases Made by Oligomerized Pool ENgineering (OPEN). Plos One *4*, e4348.

Furukawa, M.T., Sakamoto, H., and Inoue, K. (2015). Interaction and colocalization of HERMES/RBPMS with NonO, PSF, and G3BP1 in neuronal cytoplasmic RNP granules in mouse retinal line cells. Genes Cells *20*, 257–266.

Gaertner, A., Brodehl, A., and Milting, H. (2019). Screening for mutations in human cardiomyopathy- is RBM24 a new but rare disease gene? Protein Cell *10*, 393–394.

Garfinkel, A.C., Seidman, J.G., and Seidman, C.E. (2018). Genetic Pathogenesis of Hypertrophic and Dilated Cardiomyopathy. Heart Fail Clin *14*, 139–146.

Gautel, M., and Djinović-Carugo, K. (2016). The sarcomeric cytoskeleton: from molecules to motion. J Exp Biol *219*, 135–145.

Gautel, M., Zuffardi, O., Freiburg, A., and Labeit, S. (1995). Phosphorylation switches specific for the cardiac isoform of myosin binding protein-C: a modulator of cardiac contraction? Embo J *14*, 1952–1960.

Gerber, W.V., Yatskievych, T.A., Antin, P.B., Correia, K.M., Conlon, R.A., and Krieg, P.A. (1999). The RNA-binding protein gene, hermes, is expressed at high levels in the developing heart. Mechanisms of Development *80*, 77–86.

González-Rosa, J.M., Sharpe, M., Field, D., Soonpaa, M.H., Field, L.J., Burns, C.E., and Burns, C.G. (2018). Myocardial Polyploidization Creates a Barrier to Heart Regeneration in Zebrafish. Dev Cell *44*, 433-446.e7.

Gorski, P.A., Ceholski, D.K., and Hajjar, R.J. (2015). Altered Myocardial Calcium Cycling and Energetics in Heart Failure—A Rational Approach for Disease Treatment. Cell Metab *21*, 183–194.

Grassini, D.R., Lagendijk, A.K., Angelis, J.E.D., Silva, J.D., Jeanes, A., Zettler, N., Bower, N.I., Hogan, B.M., and Smith, K.A. (2018). Nppa and Nppb act redundantly during zebrafish cardiac

development to confine AVC marker expression and reduce cardiac jelly volume. Development (Cambridge, England) *145*, dev160739.

Guner-Ataman, B., Paffett-Lugassy, N., Adams, M.S., Nevis, K.R., Jahangiri, L., Obregon, P., Kikuchi, K., Poss, K.D., Burns, C.E., and Burns, C.G. (2013). Zebrafish second heart field development relies on progenitor specification in anterior lateral plate mesoderm and nkx2.5 function. Development (Cambridge, England) *140*, 1353–1363.

Guo, W., Schafer, S., Greaser, M.L., Radke, M.H., Liss, M., Govindarajan, T., Maatz, H., Schulz, H., Li, S., Parrish, A.M., et al. (2012). RBM20, a gene for hereditary cardiomyopathy, regulates titin splicing. Nat Med *18*, 766–773.

Haas, J., Frese, K.S., Peil, B., Kloos, W., Keller, A., Nietsch, R., Feng, Z., Müller, S., Kayvanpour, E., Vogel, B., et al. (2015). Atlas of the clinical genetics of human dilated cardiomyopathy. Eur Heart J *36*, 1123–1135.

Hami, D., Grimes, A.C., Tsai, H.-J., and Kirby, M.L. (2011). Zebrafish cardiac development requires a conserved secondary heart field. Development (Cambridge, England) *138*, 2389–2398.

Heim, A.E., Hartung, O., Rothhämel, S., Ferreira, E., Jenny, A., and Marlow, F.L. (2014). Oocyte polarity requires a Bucky ball-dependent feedback amplification loop. Development *141*, 842–854.

Hoogenhof, M.M.G. van den, Beqqali, A., Amin, A.S., Made, I. van der, Aufiero, S., Khan, M.A.F., Schumacher, C.A., Jansweijer, J.A., Spaendonck-Zwarts, K.Y. van, Remme, C.A., et al. (2018). RBM20 Mutations Induce an Arrhythmogenic Dilated Cardiomyopathy Related to Disturbed Calcium Handling. Circulation *138*, 1330–1342.

Hörnberg, H., Horck, F.W., Maurus, D., Zwart, M., Svoboda, H., Harris, W.A., and Holt, C.E. (2013). RNA-binding protein Hermes/RBPMS inversely affects synapse density and axon arbor formation in retinal ganglion cells in vivo. The Journal of Neuroscience : The Official Journal of the Society for Neuroscience *33*, 10384–10395.

Horsthuis, T., Houweling, A.C., Habets, P.E.M.H., Lange, F.J. de, Azzouzi, H. el, Clout, D.E.W., Moorman, A.F.M., and Christoffels, V.M. (2008). Distinct regulation of developmental and heart disease-induced atrial natriuretic factor expression by two separate distal sequences. Circulation Research *102*, 849–859.

Huisken, J., and Stainier, D.Y.R. (2007). Even fluorescence excitation by multidirectional selective plane illumination microscopy (mSPIM). Opt Lett *32*, 2608.

Huttner, I.G., Wang, L.W., Santiago, C.F., Horvat, C., Johnson, R., Cheng, D., Frieling-Salewsky, M. von, Hillcoat, K., Bemand, T.J., Trivedi, G., et al. (2018). A-Band Titin Truncation in Zebrafish Causes Dilated Cardiomyopathy and Hemodynamic Stress Intolerance. Circulation Genom Precis Medicine *11*, e002135.

Jahangiri, L., Sharpe, M., Novikov, N., González-Rosa, J.M., Borikova, A., Nevis, K., Paffett-Lugassy, N., Zhao, L., Adams, M., Guner-Ataman, B., et al. (2016). The AP-1 transcription factor component Fosl2 potentiates the rate of myocardial differentiation from the zebrafish second heart field. Development *143*, 113–122.

Jin, J.P., and Lin, J.J. (1989). Isolation and Characterization of cDNA Clones Encoding Embryonic and Adult Isoforms of Rat Cardiac Troponin T. J Biol Chem *264*, 14471–14477.

Katz, Y., Wang, E.T., Airoldi, E.M., and Burge, C.B. (2010). Analysis and design of RNA sequencing experiments for identifying isoform regulation. Nat Methods *7*, 1009–1015.

Katz, Y., Wang, E.T., Silterra, J., Schwartz, S., Wong, B., Thorvaldsdóttir, H., Robinson, J.T., Mesirov, J.P., Airoldi, E.M., and Burge, C.B. (2015). Quantitative visualization of alternative exon expression from RNA-seq data. Bioinformatics *31*, 2400–2402.

Kaufman, O.H., Lee, K., Martin, M., Rothhämel, S., and Marlow, F.L. (2018). rbpms2 functions in Balbiani body architecture and ovary fate. PLoS Genetics *14*, e1007489.

Kofuji, P., Lederer, W.J., and Schulze, D.H. (1994). Mutually exclusive and cassette exons underlie alternatively spliced isoforms of the Na/Ca exchanger. J Biol Chem *269*, 5145–5149.

Kosaka, K., Kawakami, K., Sakamoto, H., and Inoue, K. (2007). Spatiotemporal localization of germ plasm RNAs during zebrafish oogenesis. Mech Develop *124*, 279–289.

Koushik, S.V., Wang, J., Rogers, R., Moskophidis, D., Lambert, N.A., Creazzo, T.L., and Conway, S.J. (2001). Targeted inactivation of the sodium-calcium exchanger (Ncx1) results in the lack of a heartbeat and abnormal myofibrillar organization. Faseb J *15*, 1209–1211.

Langenbacher, A.D., Dong, Y., Shu, X., Choi, J., Nicoll, D.A., Goldhaber, J.I., Philipson, K.D., and Chen, J.-N. (2005). Mutation in sodium–calcium exchanger 1 (NCX1) causes cardiac fibrillation in zebrafish. P Natl Acad Sci Usa *102*, 17699–17704.

Lazic, S., and Scott, I.C. (2011). Mef2cb regulates late myocardial cell addition from a second heart field-like population of progenitors in zebrafish. Developmental Biology *354*, 123–133.

LeWinter, M.M., and Granzier, H.L. (2013). Titin Is a Major Human Disease Gene. Circulation *127*, 938–944.

Li, B., and Dewey, C.N. (2011). RSEM: accurate transcript quantification from RNA-Seq data with or without a reference genome. Bmc Bioinformatics *12*, 323.

Lin, Y.-F., Swinburne, I., and Yelon, D. (2012). Multiple influences of blood flow on cardiomyocyte hypertrophy in the embryonic zebrafish heart. Dev Biol *362*, 242–253.

Liu, J., Kong, X., Zhang, M., Yang, X., and Xu, X. (2019). RNA binding protein 24 deletion disrupts global alternative splicing and causes dilated cardiomyopathy. Protein Cell *10*, 405–416.

Livak, K.J., and Schmittgen, T.D. (2001). Analysis of relative gene expression data using real-time quantitative PCR and the 2(-Delta Delta C(T)) Method. Methods (San Diego, Calif.) *25*, 402–408.

Love, M.I., Huber, W., and Anders, S. (2014). Moderated estimation of fold change and dispersion for RNA-seq data with DESeq2. Genome Biol *15*, 550.

Ma, A.C., Lee, H.B., Clark, K.J., and Ekker, S.C. (2013). High efficiency In Vivo genome engineering with a simplified 15-RVD GoldyTALEN design. PloS One *8*, e65259.

Maatz, H., Jens, M., Liss, M., Schafer, S., Heinig, M., Kirchner, M., Adami, E., Rintisch, C., Dauksaite, V., Radke, M.H., et al. (2014). RNA-binding protein RBM20 represses splicing to orchestrate cardiac pre-mRNA processing. J Clin Invest *124*, 3419–3430.

MacLennan, D.H., and Kranias, E.G. (2003). Phospholamban: a crucial regulator of cardiac contractility. Nat Rev Mol Cell Bio *4*, 566–577.

McNamara, J.W., and Sadayappan, S. (2018). Skeletal myosin binding protein-C: An increasingly important regulator of striated muscle physiology. Arch Biochem Biophys *660*, 121–128.

Minajigi, A., Froberg, J.E., Wei, C., Sunwoo, H., Kesner, B., Colognori, D., Lessing, D., Payer, B., Boukhali, M., Haas, W., et al. (2015). A comprehensive Xist interactome reveals cohesin repulsion and an RNA-directed chromosome conformation. Science *349*, aab2276.

Mohamed, A.S., Dignam, J.D., and Schlender, K.K. (1998). Cardiac Myosin-Binding Protein C (MyBP-C): Identification of Protein Kinase A and Protein Kinase C Phosphorylation Sites. Arch Biochem Biophys *358*, 313–319.

Nakagaki-Silva, E.E., Gooding, C., Llorian, M., Jacob, A.G., Richards, F., Buckroyd, A., Sinha, S., and Smith, C.W. (2019). Identification of RBPMS as a mammalian smooth muscle master splicing regulator via proximity of its gene with super-enhancers. ELife *8*.

Niimura, H., Bachinski, L.L., Sangwatanaroj, S., Watkins, H., Chudley, A.E., McKenna, W., Kristinsson, A., Roberts, R., Sole, M., Maron, B.J., et al. (1998). Mutations in the Gene for Cardiac Myosin-Binding Protein C and Late-Onset Familial Hypertrophic Cardiomyopathy. New Engl J Medicine *338*, 1248–1257.

Notarnicola, C., Rouleau, C., Guen, L.L., Virsolvy, A., Richard, S., Faure, S., and Barbara, P.D.S. (2012). The RNA-Binding Protein RBPMS2 Regulates Development of Gastrointestinal Smooth Muscle. Gastroenterology *143*, 687-697.e9.

Paffett-Lugassy, N., Singh, R., Nevis, K.R., Guner-Ataman, B., O'Loughlin, E., Jahangiri, L., Harvey, R.P., Burns, C.G., and Burns, C.E. (2013). Heart field origin of great vessel precursors relies on nkx2.5-mediated vasculogenesis. Nat Cell Biol *15*, 1362–1369.

Panáková, D., Werdich, A.A., and MacRae, C.A. (2010). Wnt11 patterns a myocardial electrical gradient through regulation of the L-type Ca(2+) channel. Nature *466*, 874–878.

Pater, E. de, Clijsters, L., Marques, S.R., Lin, Y.-F., Garavito-Aguilar, Z.V., Yelon, D., and Bakkers, J. (2009). Distinct phases of cardiomyocyte differentiation regulate growth of the zebrafish heart. Development (Cambridge, England) *136*, 1633–1641.

Patro, R., Duggal, G., Love, M.I., Irizarry, R.A., and Kingsford, C. (2017). Salmon provides fast and bias-aware quantification of transcript expression. Nat Methods *14*, 417–419.

Poss, K.D., Wilson, L.G., and Keating, M.T. (2002). Heart Regeneration in Zebrafish. Science *298*, 2188–2190.

Power, R.M., and Huisken, J. (2017). A guide to light-sheet fluorescence microscopy for multiscale imaging. Nat Methods *14*, 360–373.

Previs, M.J., Previs, S.B., Gulick, J., Robbins, J., and Warshaw, D.M. (2012). Molecular Mechanics of Cardiac Myosin-Binding Protein C in Native Thick Filaments. Science *337*, 1215–1218.

Previs, M.J., Prosser, B.L., Mun, J.Y., Previs, S.B., Gulick, J., Lee, K., Robbins, J., Craig, R., Lederer, W.J., and Warshaw, D.M. (2015). Myosin-binding protein C corrects an intrinsic inhomogeneity in cardiac excitation-contraction coupling. Sci Adv *1*, e1400205.

Quednau, B.D., Nicoll, D.A., and Philipson, K.D. (1997). Tissue specificity and alternative splicing of the Na+/Ca2+ exchanger isoforms NCX1, NCX2, and NCX3 in rat. Am J Physiol-Cell Ph *272*, C1250–C1261.

Quinlan, A.R., and Hall, I.M. (2010). BEDTools: a flexible suite of utilities for comparing genomic features. Bioinformatics *26*, 841–842.

Refaat, M.M., Lubitz, S.A., Makino, S., Islam, Z., Frangiskakis, J.M., Mehdi, H., Gutmann, R., Zhang, M.L., Bloom, H.L., MacRae, C.A., et al. (2012). Genetic variation in the alternative splicing regulator RBM20 is associated with dilated cardiomyopathy. Heart Rhythm *9*, 390–396.

Russell, J.T. (2011). Imaging calcium signals in vivo: a powerful tool in physiology and pharmacology. Brit J Pharmacol *163*, 1605–1625.

Sander, J.D., Cade, L., Khayter, C., Reyon, D., Peterson, R.T., Joung, J.K., and Yeh, J.-R.J. (2011). Targeted gene disruption in somatic zebrafish cells using engineered TALENs. Nat Biotechnol *29*, 697–698.

Sanjana, N.E., Cong, L., Zhou, Y., Cunniff, M.M., Feng, G., and Zhang, F. (2012). A transcription activator-like effector toolbox for genome engineering. Nat Protoc *7*, 171–192.

Schneider, C.A., Rasband, W.S., and Eliceiri, K.W. (2012). NIH Image to ImageJ: 25 years of image analysis. Nature Methods *9*, 671–675.

Schoenebeck, J.J., Keegan, B.R., and Yelon, D. (2007). Vessel and blood specification override cardiac potential in anterior mesoderm. Developmental Cell *13*, 254–267.

Serbedzija, G.N., Chen, J.N., and Fishman, M.C. (1998). Regulation in the heart field of zebrafish. Development (Cambridge, England) *125*, 1095–1101.

Shen, S., Park, J.W., Lu, Z., Lin, L., Henry, M.D., Wu, Y.N., Zhou, Q., and Xing, Y. (2014). rMATS: robust and flexible detection of differential alternative splicing from replicate RNA-Seq data. Proceedings of the National Academy of Sciences of the United States of America *111*, E5593-601.

Simmerman, H.K.B., and Jones, L.R. (1998). Phospholamban: Protein Structure, Mechanism of Action, and Role in Cardiac Function. Physiol Rev *78*, 921–947.

Skrzynia, C., Berg, J., Willis, M., and Jensen, B. (2014). Genetics and Heart Failure: A Concise Guide for the Clinician. Curr Cardiol Rev *11*, 10–17.

Soneson, C., Love, M.I., and Robinson, M.D. (2016). Differential analyses for RNA-seq: transcript-level estimates improve gene-level inferences. F1000research *4*, 1521.

Thisse, C., and Thisse, B. (2008). High-resolution in situ hybridization to whole-mount zebrafish embryos. Nature Protocols *3*, 59–69.

Towbin, J.A. (2000). Molecular genetics of hypertrophic cardiomyopathy. Curr Cardiol Rep *2*, 134–140.

Towbin, J.A., and Bowles, N.E. (2000). Genetic abnormalities responsible for dilated cardiomyopathy. Curr Cardiol Rep *2*, 475–480.

Toyoshima, C., Asahi, M., Sugita, Y., Khanna, R., Tsuda, T., and MacLennan, D.H. (2003). Modeling of the inhibitory interaction of phospholamban with the Ca2+ ATPase. Proc National Acad Sci *100*, 467–472.

Virani, S.S., Alonso, A., Aparicio, H.J., Benjamin, E.J., Bittencourt, M.S., Callaway, C.W., Carson, A.P., Chamberlain, A.M., Cheng, S., Delling, F.N., et al. (2021). Heart Disease and Stroke Statistics—2021 Update: A Report From the American Heart Association. Circulation CIR0000000000000950.

Wang, G., Yang, L., Grishin, D., Rios, X., Ye, L.Y., Hu, Y., Li, K., Zhang, D., Church, G.M., and Pu, W.T. (2017). Efficient, footprint-free human iPSC genome editing by consolidation of Cas9/CRISPR and piggyBac technologies. Nat Protoc *12*, 88–103.

Wilmore, H.P., McClive, P.J., Smith, C.A., and Sinclair, A.H. (2005). Expression profile of the RNA-binding protein gene hermes during chicken embryonic development. Developmental Dynamics : An Official Publication of the American Association of Anatomists *233*, 1045–1051.

Yelon, D., Horne, S.A., and Stainier, D.Y. (1999). Restricted expression of cardiac myosin genes reveals regulated aspects of heart tube assembly in zebrafish. Developmental Biology *214*, 23–37.

Zhou, Y., Cashman, T.J., Nevis, K.R., Obregon, P., Carney, S.A., Liu, Y., Gu, A., Mosimann, C., Sondalle, S., Peterson, R.E., et al. (2011). Latent TGF-β binding protein 3 identifies a second heart field in zebrafish. Nature *474*, 645–648.

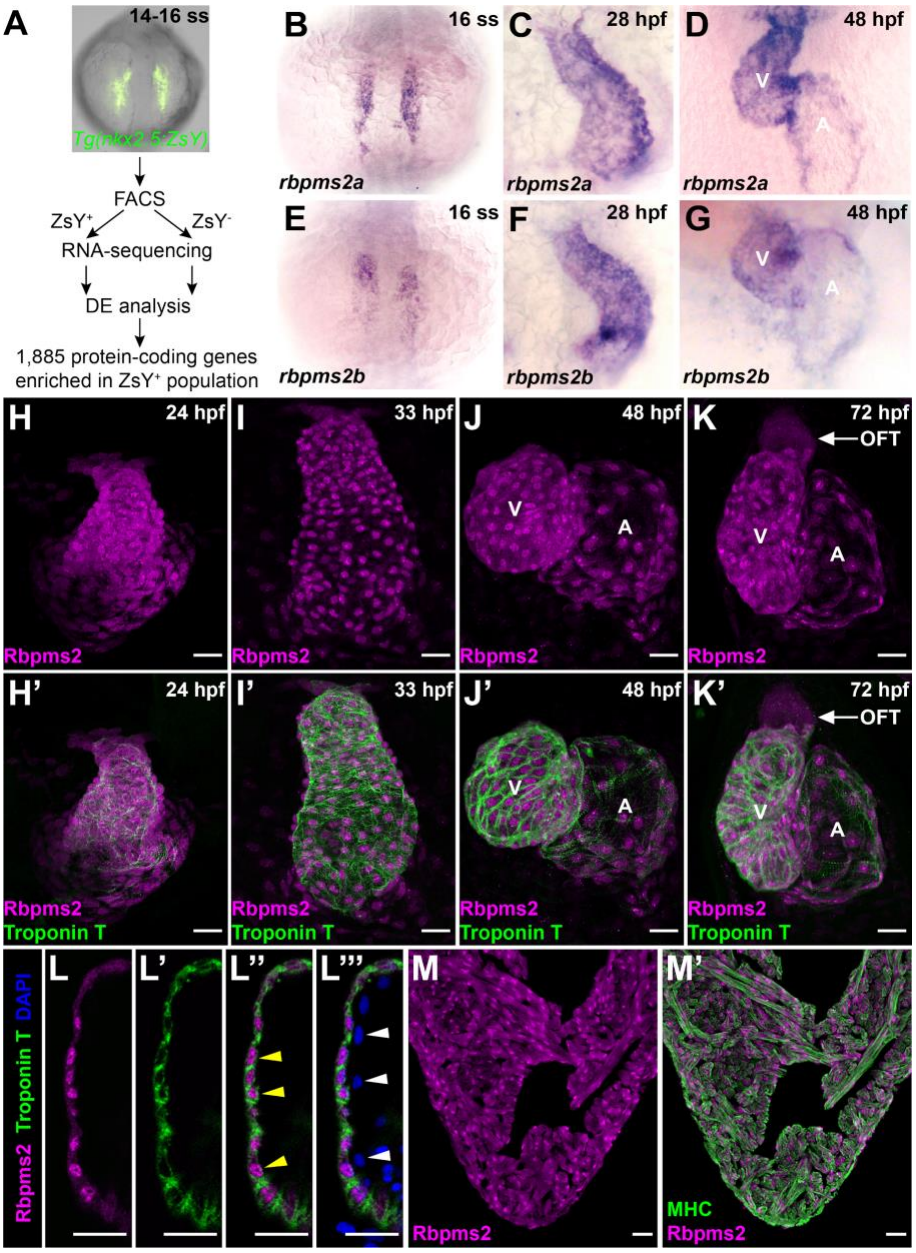

Figure 1 – Restricted expression of RNA-binding proteins Rbpms2a and Rbpms2b to the zebrafish myocardium. (A) Workflow used to identify 1848 protein-coding RNAs enriched in ZsYellow-positive (ZsY+) cardiopharyngeal progenitors or cardiomyocytes in the anterior lateral plate mesoderm of 14-16 somites stage (ss) *Tg(nkx2.5:ZsYellow)* embryos. (B-G) Brightfield images of 16 ss (B,E), 28 hours post fertilization (hpf; C,F), and 48 hpf (D,G) embryos processed for in situ hybridization with riboprobes that detect *rbpms2a* (B-D) or *rbpms2b* (E-G). Little to no variation in expression pattern was observed between animals in each group (n>10/group). (H-K') Confocal projections of hearts in 24 hpf (H,H'), 33 hpf (I,I'), 48 hpf (J,J'),

and 72 hpf (K,K') zebrafish embryos co-immunostained with antibodies that detect Rbpms2 (magenta) or cardiac Troponin T (CT3 antibody; green). Single (H,I,J,K) and merged double channel (H',I',J',K') images are shown. Little to no variation in expression pattern was observed between animals in each group (n>10/group). (L-L''') Single optical section through the ventricular wall of a 48 hpf embryo co-immunostained with antibodies that detect Rbpms2 (magenta) or cardiac Troponin T (CT3 antibody; green) and counterstained with DAPI (blue). Single (L, L'), merged double (L''), and merged triple (L''') channel images are shown. Yellow arrowheads highlight Rbpms2-positive cardiomyocyte nuclei surrounded by Troponin T-positive cytoplasm. White arrowheads highlight Rbpms2-negative nuclei in adjacent endocardial cells lining the ventricular chamber. 4/4 ventricles exhibited this Rbpms2 expression pattern. (M,M') Confocal projections of a histological section through the ventricle of an adult zebrafish heart co-immunostained with antibodies that detect Rbpms2 (magenta) or Myosin Heavy Chain (MHC; MF20 antibody; green). Single channel (M) and merged double channel (M') images are shown. 18/18 sections, 6 from each of three hearts, exhibited this Rbpms2 expression pattern. Abbreviations: FACS, fluorescence activated cell sorting, DE, differential expression; V, ventricle; A, atrium; OFT, outflow tract. Scale bars=25μm.

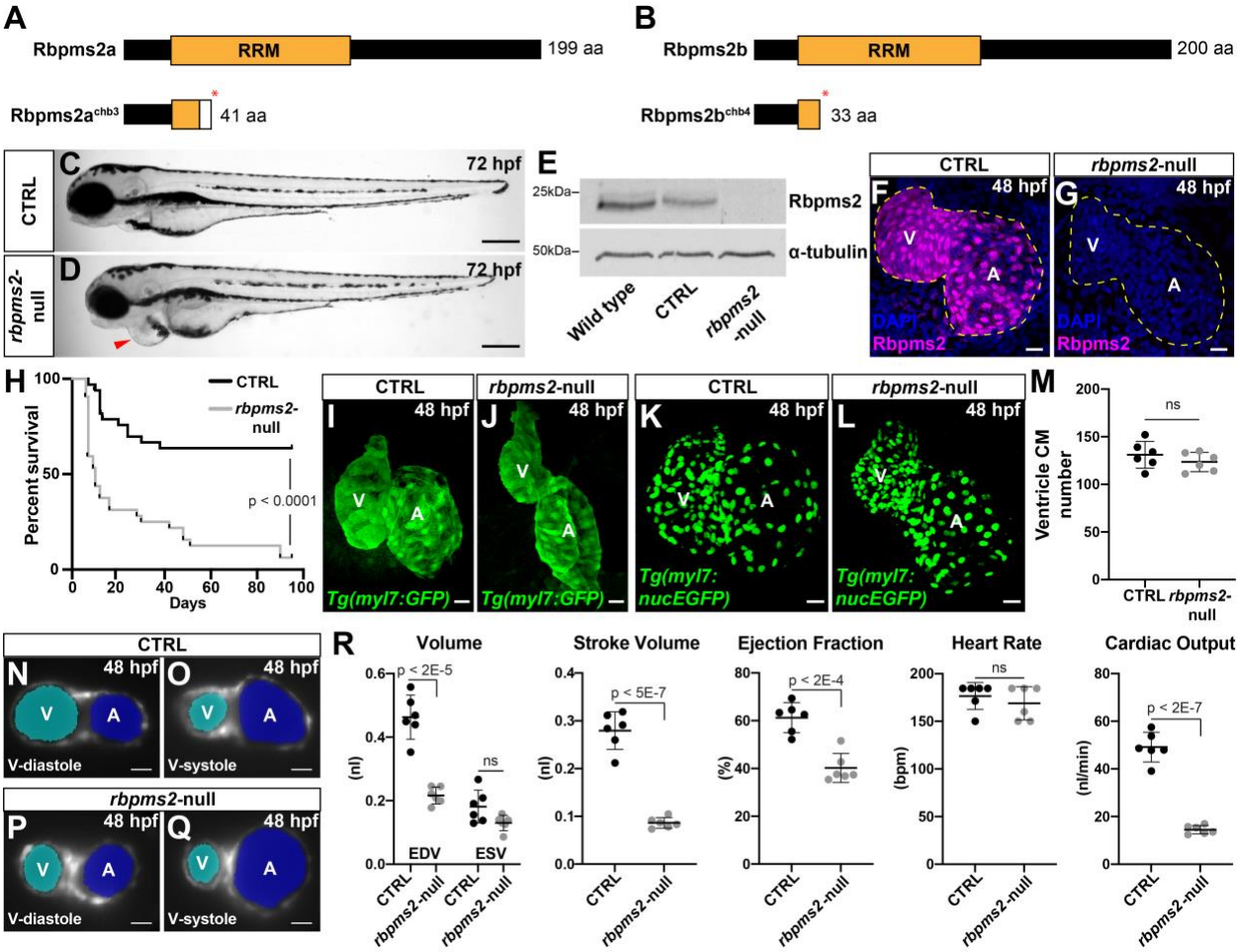

Figure 2 – *rbpms2a* and *rbpms2b* are required for ventricular function. (A,B) Schematic diagrams of Rbpms2a and Rbpms2b (top) and the predicted protein products of the *rbpms2a*^{chb3} and *rbpms2b*^{chb4} alleles (bottom). The asterisks mark the locations of premature stop codons (*) within the RNA-recognition motifs (RRMs) caused by frame-shifting deletions. The white box in (A) shows the location of divergent amino acids prior to the stop codon. (C-D) Brightfield images of control-sibling (C; CTRL) and *rbpms2*-null (*rbpms2a*$^{chb3/chb3}$; *rbpms2b*$^{chb4/chb4}$; D) embryos at 72 hours post fertilization (hpf). Arrowhead highlights pericardial edema in the mutant. Little to no variation in phenotype was observed between animals in each group (n>10/group). Scale bars=250µm. (E) Western blot showing Rbpms2 levels in 48 hpf wild-type (WT), CTRL, and *rbpms2*-null embryos (top) relative to the loading control alpha-tubulin (bottom). (F-G) Confocal projections of hearts in 48 hpf CTRL (F) and *rbpms2*-null (G) embryos immunostained with an

antibody that detects Rbpms2 (magenta) and counterstained with DAPI (blue). The dotted lines delineate the myocardium as ascertained from the Rbpms2 signal (F) or *Tg(myl7:eGFP)* reporter signal present in these animals (F,G; not shown). Little to no variation in expression pattern was observed between animals in each group (n>10/group). (H) Kaplan Meier plot showing the survival curves of CTRL (n=33) and *rbpms2*-null (n=33) animals. Statistical significance was determined using a log-rank test. (I-L) Confocal projections of hearts in 48 hpf CTRL (I,K) or *rbpms2*-null (J,L) embryos carrying the *myl7:GFP* (I,J) or *myl7:nucGFP* (K,L) transgenes immunostained with an anti-GFP antibody. For (I,J), little to no variation in phenotype was observed between animals in each group (n>10/group). (M) Dot plot showing ventricular cardiomyocyte (CM) number in CTRL (n=6) and *rbpms2*-null (n=6) hearts at 48 hpf. Error bars show one standard deviation. Statistical significance was determined by an unpaired, two-tailed Student's t-test assuming equal variances. ns, not significant. (N-Q) Single-plane light sheet fluorescence microscopy images of hearts in 48 hpf CTRL (N,O) and *rbpms2*-null (P,Q) embryos carrying the *myl7:GFP* transgene. Images of hearts during ventricular diastole (N,P) or systole (O,Q) are shown with Cardiac Functional Imaging Network (CFIN) overlays of the atrial (blue) and ventricular (cyan) lumens. (R) Dot plots showing end-diastolic volume (EDVs) and end-systolic volume (ESVs), stroke volume, ejection fraction, heart rate, and cardiac output of ventricles in 48 hpf CTRL (n=6) and *rbpms2*-null (n=6) animals measured with CFIN. Error bars show one standard deviation. Statistical significance was determined by an unpaired, two-tailed Student's t-test assuming equal variances. ns, not significant. Abbreviations: aa, amino acid; V, ventricle; A, atrium. Scale bars=25μm.

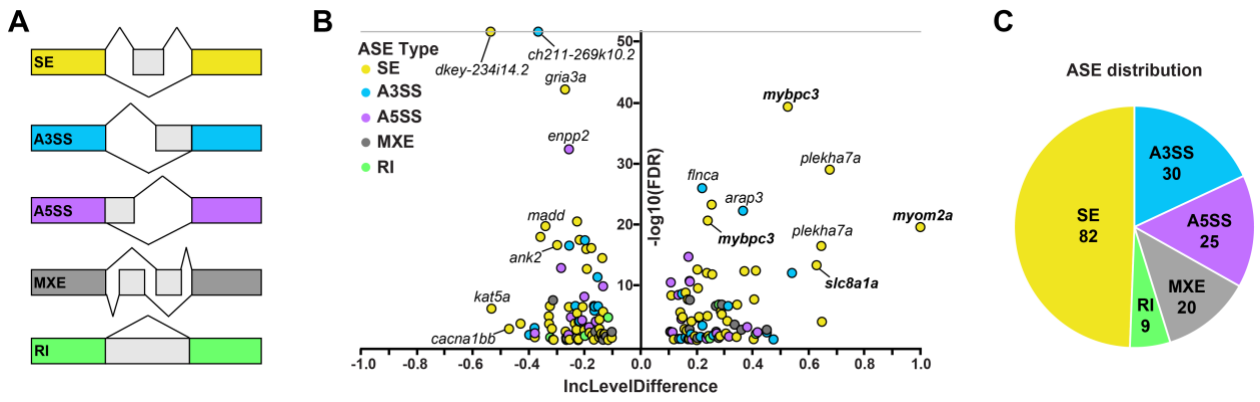

Figure 3 – Identification of differential alternative splicing events in *rbpms2*-null embryos. (A) Schematic diagrams of the categories of alternative splicing events (ASEs) investigated by the RNA-seq Multivariate Analysis of Transcript Splicing (rMATS) algorithm including skipped exon (SE), alternative 3' splice site (A3SS), alternative 5' splice site (A5SS), mutually exclusive exon (MXE), and retained intron (RI). (B) Volcano plot showing the inclusion (Inc) level differences (control-sibling Inclevel - *rbpms2*-null Inclevel) and False Discovery Rates (FDR) for differential ASEs between 33 hours post fertilization (hpf) control-sibling and *rbpms2*-null animals (0 uncalled replicates; FDR<0.01; |Incleveldifference|>0.1;). The ASEs shown in bold were validated with splicing-sensitive qPCR and in situ hybridization. (C) Pie chart showing the proportions of differential ASEs in each category in *rbpms2*-null animals.

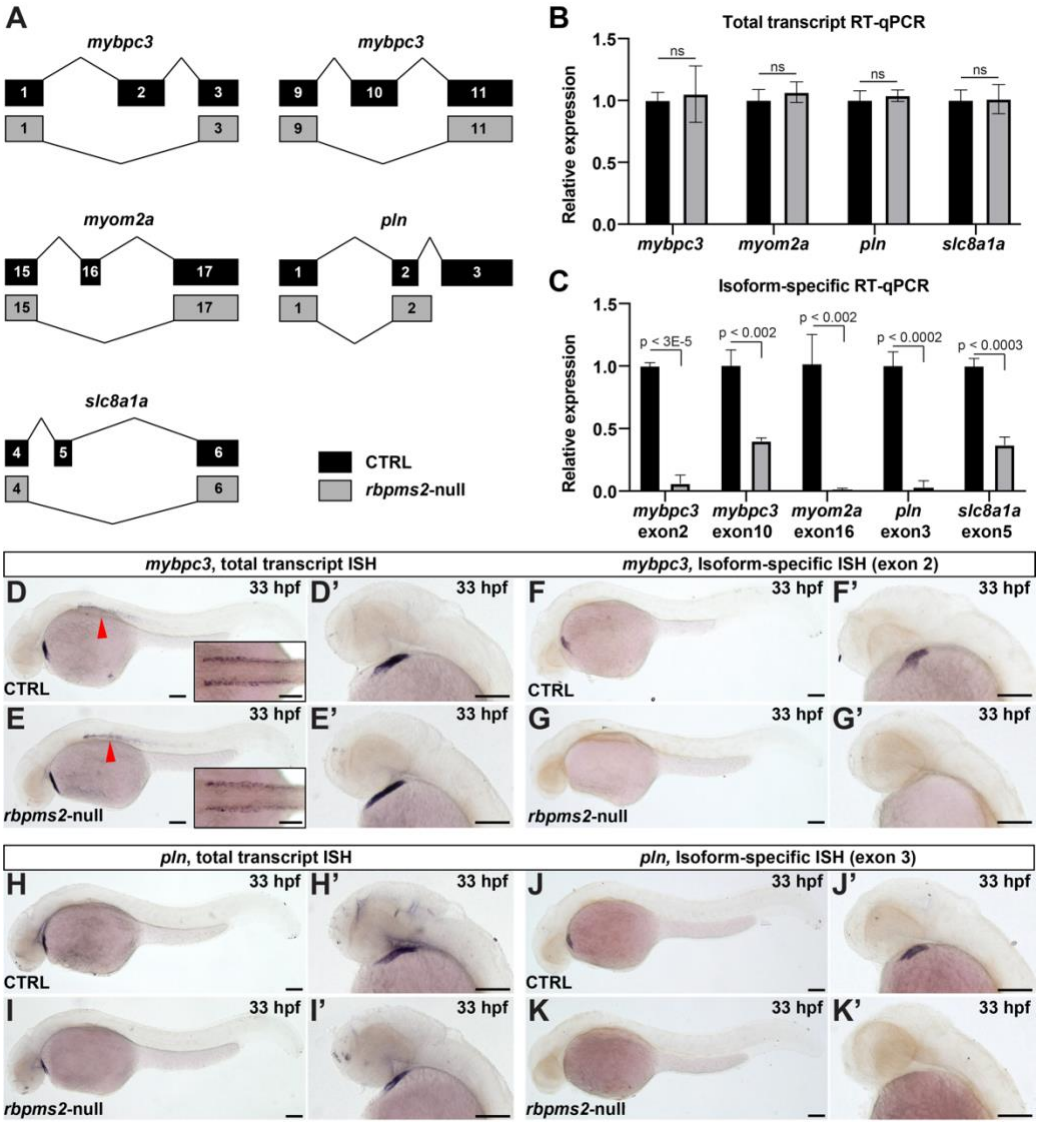

Figure 4 – Validation of differential alternative splicing events in *rbpms2*-null animals. (A) Schematic diagrams of alternative splicing events (ASEs) identified in control-sibling (CTRL) or *rbpms2*-null animals at 33 hours post fertilization (hpf) by the RNA-seq Multivariate Analysis of Transcript Splicing (rMATS) or mixture of isoforms (MISO) algorithms. The legend indicates that the isoforms shown on top (black) are significantly reduced or absent in *rbpms2*-null animals and replaced by the isoforms shown on the bottom (gray). (B) Bar graph showing the relative expression levels of the four genes shown in (A), independent of the alternatively spliced exons, between 48 hours post fertilization control-sibling and DKO animals. (C) Bar graph showing the relative expression levels of the indicated, exon-containing isoforms [(shown in black in (A)] of the same four genes between control-sibling and *rbpms2*-null animals at 48 hpf. For (B,C), error bars show one standard deviation. Statistical significance was determined by an unpaired, two-

tailed Student's t-test assuming equal variances. ns, not significant. (D-K') Brightfield images of 33 hpf CTRL (D,D',F,F',H,H'J,J') and *rbpms2*-null (E,E',G,G',I,I',K,K') embryos processed for in situ hybridization with riboprobes that detect total pools (D-E'; H-I') or specific exon-containing mRNA isoforms (F-G'; J-K') of *mybpc3* (D-G') or *pln* (H-K'). The cardiac regions in (D,E,F,G,H,I,J,K) are shown at higher zoom in (D',E',F',G',H',I',J',K'). Red arrowheads in (D,E) highlight expression of *mybpc3* in skeletal muscle, which is also shown from a dorsal view in the insets. Little to no variation in expression pattern was observed between animals in each group (n>10/group). Scale bars=100μm.

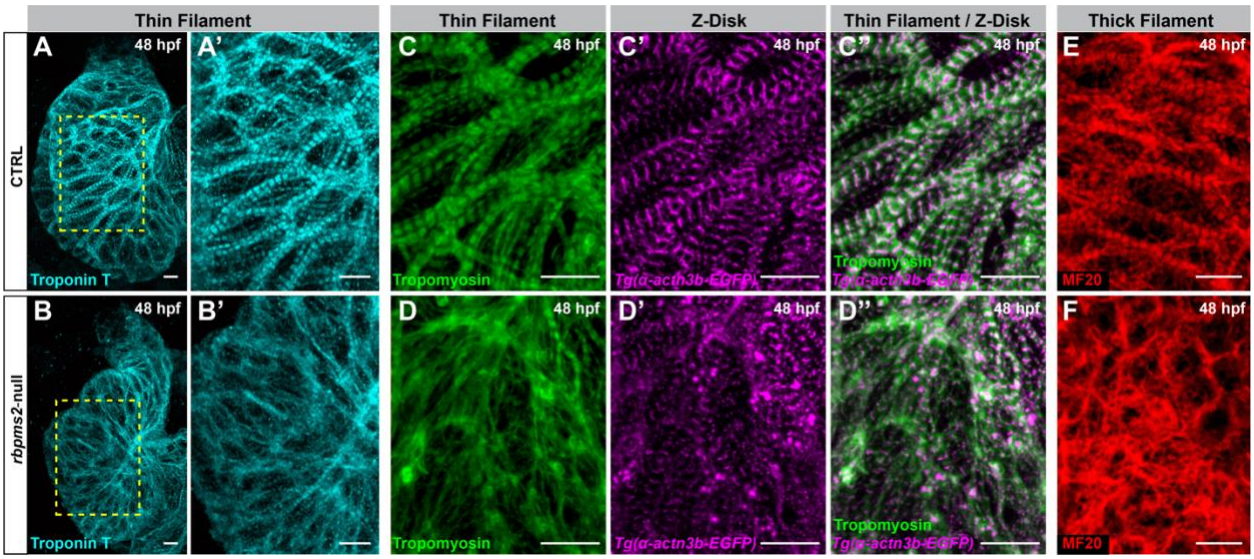

Figure 5 – Myofibrillar disarray in *rbpms2*-null ventricular cardiomyocytes. (A-B') Confocal projections of ventricles in 48 hours post fertilization (hpf) control-sibling (CTRL) or *rbpms2*-null embryos immunostained with an anti-TroponinT antibody (CT3) to visualize thin filaments. Regions demarcated in (A) and (B) are enlarged in (A') and (B'). (C-D'') Confocal projections of ventricles in 48 hpf CTRL and *rbpms2*-null *Tg(α-actn3b-EGFP)* animals co-immunostained with antibodies that detect Tropomyosin (CH1; green) to visualize thin filaments or GFP (magenta) to visualize Z-disks. (E-F) Confocal projections of ventricles in 48 hpf CTRL and *rbpms2*-null embryos immunostained with an antibody that detects myosin heavy chain (MF20) to visualize thick filaments. Little to no variation in protein distributions were observed between animals in each group (n>10 animals/group). Scale bars=10μm.

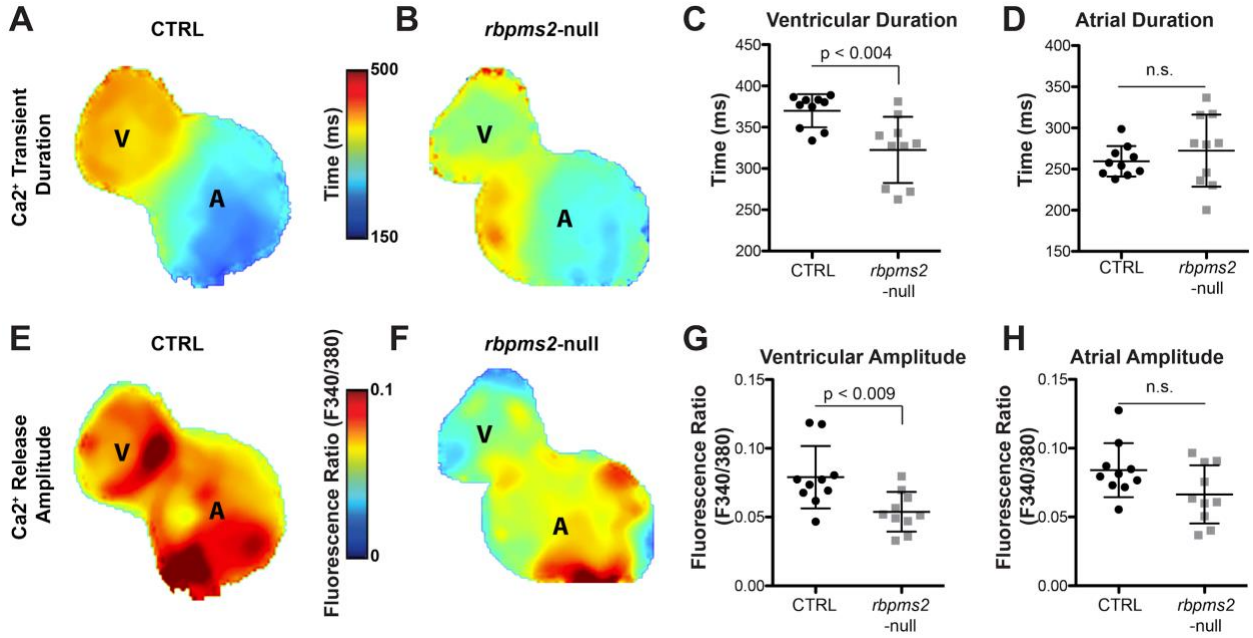

Figure 6 – *rbpms2*-null ventricular cardiomyocytes exhibit reductions in Ca2+-transient duration and amplitude. Color maps (A,B,E,F) and dot plots (C,D,G,H; n=10/group) of Ca2+-transient duration (A-D) and Ca2+ release amplitude (E-F) in the ventricle (A-C; E-G) and atrium (A,B,D,E,F,H) of 48 hours post fertilization control-sibling (CTRL; A,C,D,E,G,H) and *rbpms2*-null (B-D; F-H) hearts. Color code depicts localized Ca2+-transient duration in milliseconds (ms; A,B) or the ratiometric fluorescence indicator of Ca2+-release amplitude. Each dot represents center-chamber measurements from one heart. Error bars show one standard deviation. Statistical significance was determined by an unpaired, two-tailed Student's t-test assuming equal variances. ns, not significant.

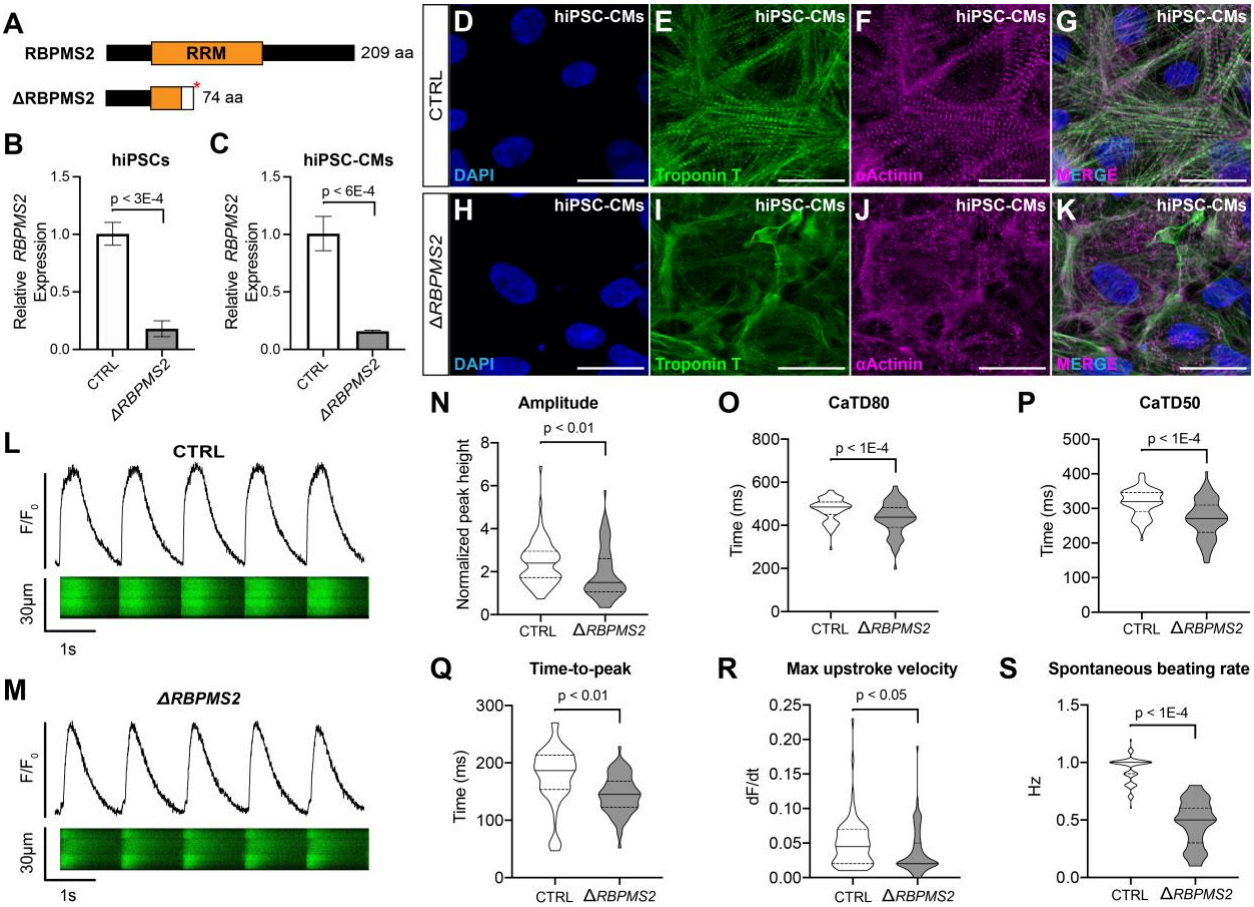

Figure 7 – Human *RBPMS2*-null cardiomyocytes exhibit myofibrillar disarray and Ca2+ handling defects similar to those in zebrafish *rbpms2*-null cardiomyocytes. (A,B) Schematic diagrams of human RBPMS2 (top) and the predicted protein product of the *ΔRBPMS2* null allele created with CRISPR/Cas9-mediated genome editing (bottom). The asterisk shows the location of a premature stop codon within the RNA-recognition motif (RRM) caused by a frame-shifting 2 base pair deletion. The white box shows the location of divergent amino acids prior to the stop codon. (B,C) Bar graphs showing the relative expression levels of *RBPMS2* in parental control (CTRL) and *ΔRBPMS2* human induced pluripotent stem cells (hiPSCs; B) and cardiomyocytes (hiPSC-CMs; C) after 15 days of directed differentiation. Error bars show one standard deviation. Statistical significance was determined by an unpaired, two-tailed Student's t-test assuming equal variances. (D-K) Representative confocal projections of CTRL (D-G) and *ΔRBPMS2* (H-K) hiPSC-CMs immunostained with antibodies that detect TroponinT (CT3; green) or Alpha Actinin (anti-Sarcomeric Alpha Actinin; magenta) to visualize thin filaments or Z-disks, respectively, and counterstained with DAPI (blue). Single (D-F; H-J) and merged triple (G,K) channel images are shown. Little to no variation in staining pattern was observed between cells in each experimental group (n>50 cells/group from at least three wells

from two separate differentiations were examined). (L,M) Representative traces of fluorescence intensity over baseline (F/F_o; top) derived from line scans (bottom) of CTRL (L) and *ΔRBPMS2* (M) hiPSC-CMs loaded with fluo-4 and paced at 1Hz. (N-S) Violin plots showing Ca2+-transient amplitude (N), duration at 80% (O) and 50% (P) repolarization, time to peak amplitude (Q), upstroke velocity (R), and un-paced spontaneous beating rate (S). Statistical significance was determined by an unpaired, two-tailed Student's t-test assuming equal variances. n=80 cells/group, 40 each from two separate differentiations. Scale bars=25μm.